Editors' Suggestion

Large anomalous Nernst effect and its bipolarity in the quaternary equiatomic Heusler alloys CrRuXGe (X = Co and Mn)

Amit Chanda [1,*] Jadupati Nag [2,3] Noah Schulz [1] Aftab Alam [2] K. G. Suresh [2] Manh-Huong Phan,[1] and Hariharan Srikanth [1,†]

[1]*Department of Physics, University of South Florida, Tampa, Florida 33620, USA*
[2]*Magnetic Materials Laboratory, Department of Physics, Indian Institute of Technology Bombay, Mumbai 400076, India*
[3]*Materials Research Institute and Department of Materials Science and Engineering, Pennsylvania State University, University Park, Pennsylvania 16802, USA*

Here we report on a comprehensive investigation of transverse magnetothermoelectric properties of the equiatomic quaternary Heusler alloys CrRuXGe (X = Co and Mn). Magnetic measurements reveal the presence of a glassy magnetic ground state owing to the energetically competing ferromagnetic and antiferromagnetic phases in CrRuCoGe at low temperatures, whereas CrRuMnGe exhibits soft ferromagnetic behavior with a weak martensitic transformation close to room temperature. The temperature-dependent anomalous Nernst coefficient (S_{ANE}) of CrRuMnGe shows noticeable changes around the martensitic transformation. While CrRuCoGe exhibits positive S_{ANE}, CrRuMnGe exhibits negative S_{ANE} throughout the measured temperature range. We demonstrate that the contribution of the anomalous transverse thermoelectric conduction dominates that of the anomalous Hall effect acting on the thermally generated carrier flow induced by the longitudinal Seebeck effect, which gives rise to the opposite polarity of S_{ANE} in these two alloys. Our detailed analysis indicates that the origin of the observed anomalous Nernst effect (ANE) in both of these alloys is dominated by the asymmetric skew scattering of charge carriers in the measured temperature regime. The sign change and tunability of ANE presented in this study provide a step forward toward the development of ANE-based efficient thermopile devices operating at room temperature utilizing the equiatomic quaternary Heusler alloys.

I. INTRODUCTION

In the last few years, there has been a significant advancement in the field of spin caloritronics which combines spintronics and thermoelectricity, and has emerged as a promising research direction for large area energy harvesting [1]. Spin caloritronics is a vast field that comprises a wide range of magnetothermoelectric phenomena, including the spin Seebeck effect (SSE) [2,3], the spin Nernst effect [4], the spin Peltier effect (SPE) [5], the anomalous Nernst effect (ANE) [6], the anomalous Ettingshausen effect (AEE) [7], etc. The ANE refers to a transverse magnetothermoelectric phenomenon in which a transverse electric voltage is generated in a conducting/semiconducting material with a spontaneous magnetization orthogonal to both the applied thermal gradient and the magnetization of the material. Unlike the ordinary Nernst effect, which is proportional to the applied magnetic field, the transverse voltage generated due to ANE is proportional to the spontaneous magnetization of the material [8]. Since the electrical voltage generated due to ANE is too low to use in practical applications, a wide range of magnetic materials has been investigated

so far, with the aim of enhancing the anomalous Nernst conductivity, namely, hole-doped manganites La$_{1-x}$Na$_x$MnO$_3$ [9], ferromagnetic cobaltites La$_{1-x}$Sr$_x$CoO$_3$ [10–12], spin-gapless semiconductors Co$_{1-x}$Fe$_{1+x}$CrGa [13], ferrimagnetic Fe$_3$O$_4$ [14], Mn-based nitrides [15], Heusler alloy based ferromagnetic shape memory alloy Ni$_2$MnGa [16], topological Heusler ferromagnet Co$_2$MnGa [17,18], topological kagome magnet Fe$_3$Sn$_2$ [19,20], correlated noncentrosymmetric kagome ferromagnet UCo$_{0.8}$Ru$_{0.2}$Al [21], polycrystalline topological ferromagnet Fe$_x$Ga$_{4-x}$ [22], ferromagnetic Weyl semimetal Co$_3$Sn$_2$S$_2$ [23,24], semimetallic polycrystalline Heusler ferromagnet CoFeVSb [25], ferrimagnetic nodal-line semiconductor Mn$_3$Si$_2$Te$_6$ [26], two-dimensional topological van der Waals ferromagnets [27,28], chiral [29] and canted [30] topological antiferromagnets, etc. Among them, topological ferromagnets exhibit the largest anomalous Nernst conductivities (≈ 0.5–$5\,\mathrm{A\,m^{-1}\,K^{-1}}$), and the origin of such colossal ANE has been shown to be due to not only the magnetization scaling of the ANE, but also the intrinsic contribution due to the existence of nonzero Berry curvature at the Fermi energy [18,23,31]. In addition to the aforementioned intrinsic mechanism, extrinsic mechanisms—for example, asymmetric skew scattering of charge carriers—also give rise to the large anomalous Nernst conductivity in Fe$_3$O$_4$ [14], hole-doped manganites La$_{1-x}$Na$_x$MnO$_3$ [9], ferromagnetic cobaltites [10–12], spin-gapless semiconductors Co$_{1-x}$Fe$_{1+x}$CrGa [13], etc.

*achanda@usf.edu
†sharihar@usf.edu

Over the past few decades, magnetic Heusler alloys have been investigated extensively due to their high Curie temperatures, large spin polarization, and tunable magnetoelectronics, which has resulted in intense interest in these materials for potential applications in spintronics [32,33]. Among the vast family of Heusler alloys, equiatomic quaternary Heusler alloys exhibit a wide range of exotic magnetoelectronic properties, e.g., half-metallicity [34,35], spin-gapless semiconducting state [36–38], spin-valve behavior [39], spin semimetallic and Weyl semimetallic behavior [40,41], etc., in combination with extraordinary thermoelectric performance [13,25,34]. The ANE has been extensively studied in full Heusler alloys, such as Co_2MnGa [17,18], Co_2TiSn [42], Co_2MnSi [43], Ni_2MnGa [16], $Ni_{46.5}Co_2Mn_{37}Sn_{14.5}$ [44], $Co_2Fe_{0.4}Mn_{0.6}Si$ [45], Cu_2CoSn [46], $Co_2MnAl_{1-x}Si_x$ [47], etc. In contrast to the full Heusler alloys, the ANE in equiatomic quaternary Heusler alloys has been rarely explored. We have recently explored transverse magnetothermoelectric properties of quaternary Heusler alloy based spin-gapless semiconductors $Co_{1-x}Fe_{1+x}CrGa$ [13,48] and semimetallic CoFeVSb [25], both of which exhibit the large anomalous Nernst thermopowers arising from both extrinsic and intrinsic origins. Moving forward, we have continued our search for multifunctional quaternary Heusler alloys with exotic magnetic properties and more efficient thermospin effects by exploiting spin degrees of freedom of this novel class of materials.

Like the thermoelectric generators based on the Seebeck thermopiles composed of conventional *p*-type and *n*-type semiconductors with opposite polarities of the longitudinal Seebeck coefficients, a recent study demonstrates the possibility of constructing ANE-based efficient thermopile devices by exploiting the bipolar nature of the ANE coefficient [49]. Note that ANE-based thermopile devices are more advantageous than the conventional Seebeck effect based thermopile devices because of the following reasons. While the Seebeck effect based thermopile devices are composed of coupled *n*- and *p*-type legs and assembled pairs [50], ANE-based thermopiles can be constructed using a simple module assembly without any complex electrical connections [30,49]. Unlike the Seebeck-based thermopiles, the electrodes used as the voltage probes in the ANE-based thermopiles can be constructed at one of the isothermal planes (typically the cold end of the thermopile assembly) [30]. Furthermore, unlike the Seebeck-based thermopiles, the output voltage of the ANE-based thermopile device scales with the dimensions of the device [30]. Therefore, combining materials with large positive and negative ANE coefficients would lead to the development of large scale ANE-based thermopile devices with highly efficient thermoelectric conversion [30]. However, despite the large number of reports on positive ANE, there are only limited reports of negative ANE [49,51–56]. Recently, the large negative ANE coefficient originating from the intrinsic Berry curvature has been observed in the topological Weyl ferromagnet $Co_3Sn_2S_2$-based alloy films where the bipolarity of ANE was achieved by tuning the Fermi level through nickel/indium substitution while retaining the topological band feature of this Weyl ferromagnet [49]. However, the Curie temperatures of most of these materials showing negative ANE are far below 300 K and hence they cannot

be used for room temperature ANE-based thermopile device applications. In this regard, magnetic Heusler alloys with high Curie temperatures and large spin polarizations [32,33] would be promising candidates for room temperature ANE-based thermopile device applications.

Here, we perform a comprehensive investigation of ANE in the equiatomic quaternary Heusler alloys CrRu*X*Ge (*X* = Co or Mn). We find that the sign of the anomalous Nernst coefficient for CrRuMnGe is opposite to that of CrRuCoGe; i.e., CrRuCoGe shows a positive anomalous Nernst coefficient (S_{ANE}) whereas CrRuMnGe exhibits a negative S_{ANE}, which has been attributed to the dominating contribution of the anomalous transverse thermoelectric conduction. Our detailed analysis indicates that the origin of the observed ANE in both these samples is dominated by the asymmetric skew scattering of charge carriers in the measured temperature regime.

II. EXPERIMENTAL SECTION

Polycrystalline samples of CrRu*X*Ge (*X* = Co and Mn) were synthesized by the arc melting technique. The synthesis methods used for these samples are reported elsewhere [36,57,58]. The crystal structure of these samples was characterized by x-ray diffraction (XRD) pattern at room temperature using an X'Pert Pro diffractometer with Cu *Kα* radiation ($\lambda = 1.54184$ Å). Temperature-dependent atomic force microscopy (AFM) scans were performed on a Hitachi 5300E environmental control system. After each scan a polynomial background and horizontal line arrangement was performed to remove any scan artifacts. From each scan, the two-dimensional (2D) autocorrelation spectra were computed. The static magnetic measurements of the samples were performed using a vibrating sample magnetometer (VSM) attached to a physical property measurement system (PPMS) from Quantum Design, USA. The longitudinal dc electrical resistivity (ρ_{xx}) and Hall resistivity (ρ_{xy}) of these samples were measured by employing the standard four-probe technique using the dc resistivity option of the PPMS. A constant dc current, $I_{dc} = 8$ mA, was sourced through the current leads while measuring ρ_{xx} of these samples. The longitudinal thermopower (S_{xx}) and thermal conductivity (κ_{xx}) of these samples were simultaneously measured using the thermal transport option (TTO) of the PPMS. Samples with dimensions $5 \times 4 \times 2$ mm^3 (for CrRuCoGe) and $5 \times 4 \times 1.75$ mm^3 (for CrRuMnGe) were used for dc resistivity, Hall, TTO, and Nernst measurements.

The Nernst measurements on the CrRu*X*Ge (*X* = Co and Mn) samples were performed as a function of temperature and magnetic field by using a home-built spin-caloritronic measurement setup integrated with the PPMS. The spin-caloritronic measurement setup is based on a universal sample puck for the PPMS. The samples under consideration were sandwiched between two copper blocks in such a way that the temperature gradient (along the thickness of the sample) generated by the two copper blocks is transverse to the direction of the applied dc magnetic field. While the bottom copper block (hot) was thermally separated from the PPMS puck base by a Teflon block, the top copper block (cold) was thermally linked to the PPMS puck base by a pair of molybdenum screws. A layer of Kapton tape was thermally anchored to the
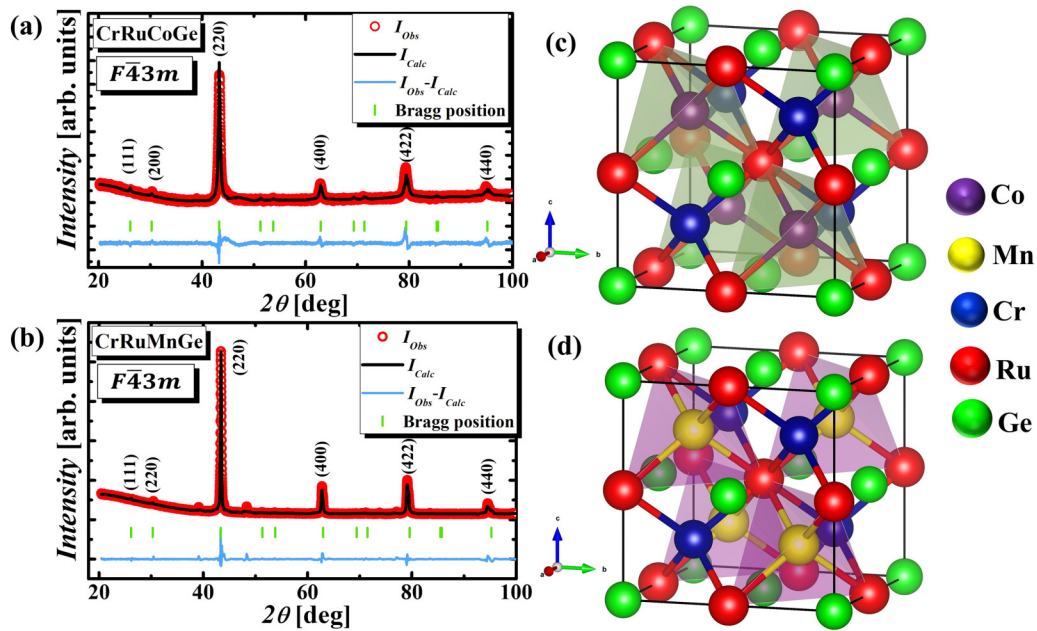
FIG. 1. X-ray diffraction (XRD) patterns for (a) CrRuCoGe, and (b) CrRuMnGe, respectively, along with the Rietveld analysis. Schematic representations of the crystal structures of CrRuCoGe and CrRuMnGe are shown in (c), (d), respectively.

bare surfaces of both copper blocks to ensure that the top and bottom surfaces of the sample was electrically insulated from the copper blocks. Each of these copper blocks was equipped with a Pt100 RTD sensor (serving as a resistive heater) and a calibrated Si-diode thermometer. Note that the thermometers were attached to the closest proximity of the sample surface to ensure accurate temperature readings of the hot and cold surfaces of the sample. Furthermore, a thin layer of Apiezon N grease was applied to the Kapton tape anchored to the bare surfaces of the copper blocks for better thermal connectivity between the sample surfaces and the hot/cold copper blocks. The temperatures of both copper blocks were controlled and monitored using two distinct temperature controllers (Scientific Instruments 9700). The drop in temperature gradient in the N grease layers on both sides of the sample and the roles of the interfacial thermal resistances between the hot/cold copper blocks and the N grease layers—as well as the interfacial thermal resistances between the sample surfaces and the N grease layers on the effective temperature gradient across the sample—have been briefly described in the Results and Discussion section of this paper. The Nernst voltage generated in the presence of the applied temperature gradient and external magnetic field produced by the superconducting magnet of the PPMS was recorded using a Keithley 2182A nanovoltmeter. A more detailed description of our spin-calorimetric measurement setup is reported elsewhere [13,25].

III. RESULTS AND DISCUSSION

Figures 1(a) and 1(b) show the room temperature XRD patterns for the CrRuCoGe and CrRuMnGe samples, respectively, along with the Rietveld analysis performed using FULLPROF SUITE software. Both samples adopt a cubic crystal structure with space group $F\bar{4}3m$ associated with the structural prototype of LiMgPdSn. The lattice parameters of CrRuCoGe and CrRuMnGe are 5.9048(8) and 5.8976(2) Å, respectively. The superlattice peaks (111) and (200) are visible for both CrRuCoGe and CrRuMnGe, indicating the presence of the ordered phases. In the case of equiatomic quaternary Heusler alloys with the composition $XX'YZ$, there exist three different nondegenerate (types I, II, and III) structural configurations depending on the four constituent atoms occupying the four different Wyckoff positions at $4a$ (0, 0, 0), $4b$ ($\frac{1}{2}$, $\frac{1}{2}$, $\frac{1}{2}$), $4c$ ($\frac{1}{4}$, $\frac{1}{4}$, $\frac{1}{4}$), and $4d$ ($\frac{3}{4}$, $\frac{3}{4}$, $\frac{3}{4}$) [35]. From the first-principles electronic-structure calculations, it was previously shown by different groups that the type I configuration is the most energetically favorable one for most of the equiatomic quaternary Heusler alloys [36,57,59]. Schematic representations of the crystal structures of CrRuCoGe and CrRuMnGe are shown in Figs. 1(c) and 1(d), where Cr, Ru, Co(Mn), and Ge atoms occupy the Wyckoff positions of $4a$, $4b$, $4c$, and $4d$ considering type I structure [57,60]. Interestingly, two additional peaks at $\approx 40°$ and $50°$ are visible in the XRD spectra for CrRuMnGe, which are not primary $F\bar{4}3m$ cubic peaks, rather originating from a weak secondary cubic and nonmagnetic Cr_3Ge phase ($\sim$5%) [61]. The average crystal grain size (D) was estimated using the Scherrer equation [62], $D = \frac{K\lambda}{m\cos\theta}$, where λ = wavelength of the x ray, θ = diffraction angle, m = full width at half maximum of the diffraction peak, and K refers to the Scherrer constant. Considering $\lambda = 1.5418$ Å, $K = 0.89$ [62], and the diffraction peak at $2\theta = 43.3°$ for both samples, we obtained $D = (23 \pm 1)$ and (41 ± 3) nm for CrRuCoGe and CrRuMnGe, respectively.

Figures 2(a) and 2(b) show the temperature dependence of magnetization, $M(T)$ of CrRuCoGe and CrRuMnGe, respectively, measured in the presence of an external magnetic field of $\mu_0 H = 0.01$ T under the zero field cooled warming (ZFCW), field cooled cooling (FCC), and field cooled warming (FCW) protocols in the temperature range 10 K ⩽
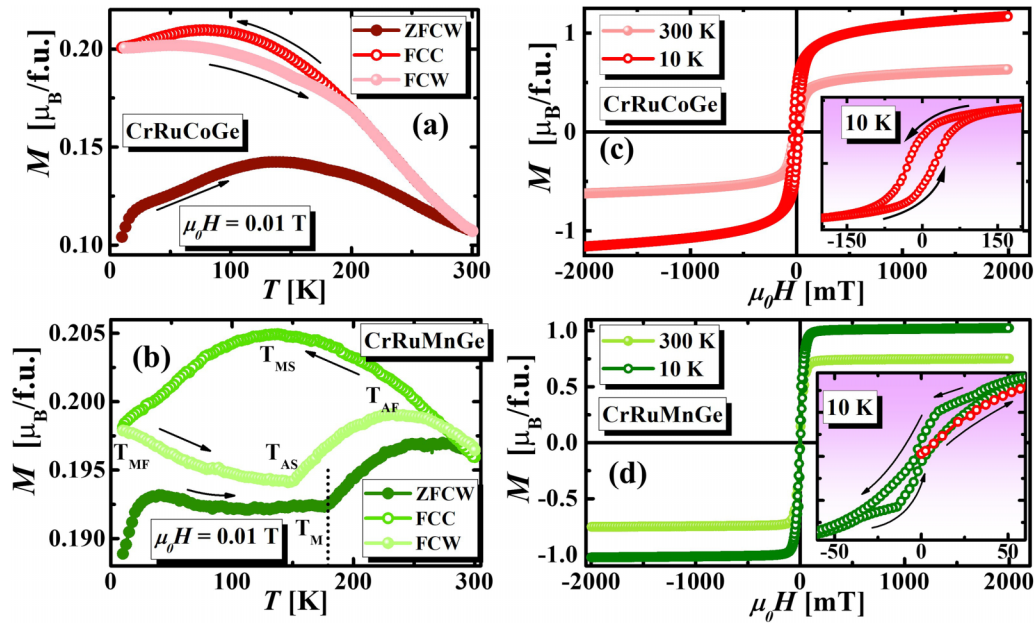
FIG. 2. Temperature dependence of magnetization $M(T)$ of (a) CrRuCoGe, and (b) CrRuMnGe, respectively, measured in the presence of an external magnetic field of $\mu_0 H = 0.01$ T under the zero field cooled warming (ZFCW), field cooled cooling (FCC), and field cooled warming (FCW) protocols in the temperature range 10 K $\leqslant T \leqslant$ 300 K. For CrRuMnGe, the maximum and diplike features in the FCW $M(T)$ curve are associated with the austenite finish (T_{AF}) and start (T_{AS}) temperatures (on warming), and those in the FCC $M(T)$ are referred to as martensitic start (T_{MS}) and finish (T_{MF}) temperatures (on cooling). Magnetic field dependence of magnetization $M(H)$ for (c) CrRuCoGe, and (d) CrRuMnGe at 300 and 10 K, insets show the low field $M(H)$ behavior at 10 K. The virgin curve for CrRuMnGe at $T = 10$ K is represented by open red symbols in (d).

$T \leqslant 300$ K. A clear distinction has been observed among the ZFCW, FCC, and FCW $M(T)$ curves for the CrRuCoGe sample. Both the FCC and FCW $M(T)$ curves bifurcate from the ZFCW $M(T)$ below 300 K, and a noticeable thermal hysteresis is present between the FCC and FCW $M(T)$ curves. Additionally, the ZFCW $M(T)$ shows a broad maximum around 140 K followed by the appearance of a clear drop below 20 K. Such large bifurcation between the FCW and ZFCW $M(T)$ curves is indicative of the presence of the glassy magnetic phase (spin glass or cluster glass) at low temperatures [63,64]. The appearance of the drop in ZFCW $M(T)$ below 20 K signifies the presence of energetically competing ferromagnetic (FM) and antiferromagnetic (AFM) phases in the system. The coexistence of the competing FM and AFM states gives rise to magnetic frustration which eventually leads to the appearance of the glassy magnetic ground state at low temperatures, as observed in the quaternary Heusler alloy FeRuMnGa [63]. We noticed that the bifurcation between the FC and ZFC curves gets suppressed significantly and the thermal hysteresis gradually disappears with increasing magnetic field strength [see Figs. 3(a) and 3(b)], both of which support the presence of the glassy magnetic phase at low temperatures [65]. The glassy magnetic ground state (spin-glass or cluster-glass states) can be confirmed from the dc magnetometry measurements [66,67]. For a canonical spin-glass system, the temperature corresponding to the maximum in the ZFC $M(T)$ curve (T_{max}) obeys the de Almeida–Thouless (AT) line [66]; i.e., T_{max} shifts to the lower temperature with increasing magnetic field strength and, for low fields, the magnetic field dependence of the freezing temperature T_{max} follows the expression $H^{2/3} \propto [1 - \frac{T_{max}(H)}{T_{max}(H=0)}]$, where $T_{max}(H = 0)$ is

the zero field freezing temperature [68]. As shown in the inset of Fig. 3(b), T_{max} for our CrRuCoGe sample shows $H^{2/3}$ dependence for low fields ($\mu_0 H \leqslant 0.1$ T) indicating the presence of spin-glass-like freezing at low temperatures. The disappearance of the drop in ZFCW $M(T)$ below 20 K with increasing magnetic field strength signifies the occurrence of field induced transformations of the AFM and glassy magnetic phases to the FM phase at low temperatures.

Figure 2(c) displays the magnetic field dependence of magnetization, $M(H)$, measured at $T = 300$ and 10 K for CrRuCoGe. It is evident that the isothermal $M(H)$ curve does not fully saturate even at 10 K, which rules out the presence of the only ferromagnetic ground state in the sample. It is apparent that the $M(H)$ curve at 10 K in the high field region consists of a linear combination of an AFM-like field-linear behavior and a FM-like saturation behavior supporting the fact that the magnetic ground state of this sample is composed of competing FM and AFM components leading to the formation of a glassy magnetic state [63]. Upon a closer look [see inset of Fig. 2(c)], it appears that $M(H)$ loops at both $T = 300$ and 10 K exhibit a small hysteresis with coercive fields: $\mu_0 H_C = 22.5$ and 27.5 mT, respectively. The experimental value of saturation magnetization for CrRuCoGe at 10 K is $M_S \approx 1.15$ μ_B/f.u., which is much smaller than the value of M_S ($= 3$ μ_B/f.u.) theoretically estimated using the Slater-Pauling rule [69]. A large difference in the theoretical ($= 2$ μ_B/f.u.) and experimental ($= 0.8$ μ_B/f.u.) M_S values has also been observed in the quaternary Heusler alloy FeRuMnGa [63]. Such a discrepancy between the theoretical and experimental M_S values can be associated with the presence of the glassy magnetic phase in our CrRuCoGe sample at low
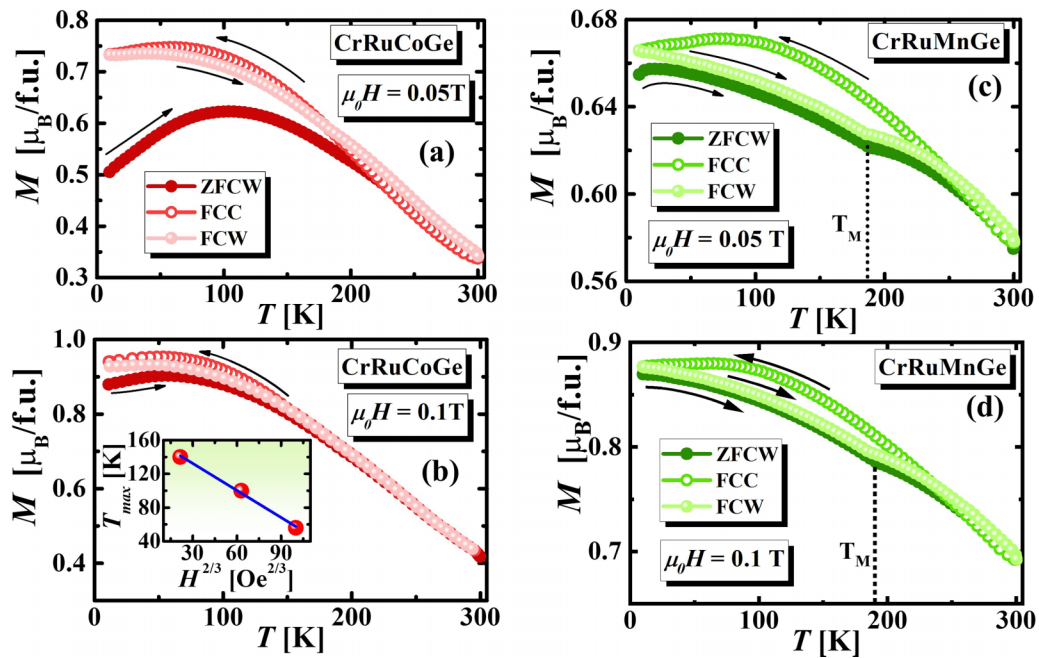
FIG. 3. $M(T)$ of CrRuCoGe in the presence of an external magnetic field of (a) $\mu_0 H = 0.05$ T, and (b) $\mu_0 H = 0.1$ T. Inset of (b) shows $H^{2/3}$ dependence of $T_{\max}$ for our CrRuCoGe sample. $M(T)$ of the CrRuMnGe sample in the presence of external magnetic field of (c) $\mu_0 H = 0.05$ T, and (d) $\mu_0 H = 0.1$ T.

temperatures, which is consistent with the observation of large bifurcation between the ZFCW and FCW $M(T)$ curves.

On the contrary, the ZFCW, FCC, and FCW $M(T)$ curves for CrRuMnGe [Fig. 2(b)] show very different behavior than CrRuCoGe. The ZFCW $M(T)$ curve for CrRuMnGe increases upon cooling from 300 K and shows a broad maximum around 250 K, which is followed by the appearance of a pronounced dip around $T_M = 180$ K. Upon further lowering temperature, the ZFCW $M(T)$ curve shows an abrupt drop below 35 K. Such a drop in the ZFCW $M(T)$ curve may originate due to the existence of a weak AFM phase in addition to the dominant FM phase. The FCW $M(T)$ curve shows behavior like the ZFCW $M(T)$ curve, except for the fact that the FCW $M(T)$ curve does not show any drop at low temperatures; instead it increases gradually down to the lowest temperature. It is also noteworthy that the high temperature maximum and the sharp dip occur at lower temperatures in the FCW $M(T)$ curve as compared to the ZFCW $M(T)$ curve. A similar trend of the ZFCW and FCW $M(T)$ curves has also been observed in the quaternary Heusler alloy $Co_{1.5}MnFe_{0.5}Si$, which was attributed to the presence of the martensitic phase [70]. Due to the diffusionless rearrangement of atoms in a material, the high temperature cubic austenite phase transforms into the low temperature tetragonal martensitic phase with lower crystal symmetry, and this transformation is known as a martensitic transformation [71]. In the vicinity of the martensitic transformation, the material undergoes a first-order magnetostructural transition and, due to the lattice mismatch between the two structurally distinct phases and the associated energy barrier, the FCC and FCW $M(T)$ curves exhibit a thermal hysteresis [72,73].

Interestingly, the FCC $M(T)$ curve for the CrRuMnGe alloy exhibits a broad maximum around ≈ 150 K and then decreases gradually down to the lowest temperature.

Furthermore, a large thermal hysteresis can be seen between the FCC and FCW $M(T)$ curves, which possibly originates due to martensitic transformation [73,74]. The maximum and diplike features in the FCW $M(T)$ curve are associated with the austenite finish (T_{AF}) and start (T_{AS}) temperatures (on warming), and those in the FCC $M(T)$ are referred to as martensitic start (T_{MS}) and finish (T_{MF}) temperatures (on cooling), [73] as indicated in Fig. 2(b). Note that the width of the thermal hysteresis around the martensitic transformation in CrRuMnGe is relatively larger and the change in magnetization (ΔM) around the transformation is comparatively smaller than those observed in Ni-Mn-Al-Co and Ni-Mn-Sn-Co Heusler alloys, [44,73] indicating the occurrence of relatively weaker martensitic transformation in CrRuMnGe. In other words, we believe that a fraction of the cubic austenite phase is getting transformed into the tetragonal martensitic phase in CrRuMnGe. The thermal hysteresis curves as well as the bifurcation between the ZFCW and FCW $M(T)$ curves (thermomagnetic irreversibility) decrease significantly with increasing the field strength up to $\mu_0 H = 0.1$ T, as shown in Figs. 3(c) and 3(d). Additionally, the features associated with the martensitic phase transition are suppressed by increasing the magnetic field strength; however, they do not disappear completely. To have a deeper insight into the bifurcation between ZFCW and FCW $M(T)$ curves as a function of magnetic field strength, we show the ZFCW, FCC, and FCW $M(T)$ curves measured under different field strengths between $\mu_0 H = 1$ and 9 T in Figs. 4(a)–4(e). It is evident that the features associated with the martensitic phase transition are present even at a high magnetic field of $\mu_0 H = 9$ T. Furthermore, the bifurcation between the ZFCW and FCW $M(T)$ curves almost disappears for $\mu_0 H = 1$ T but reappears for $\mu_0 H \geqslant 2$ T. In fact, the degree of bifurcation between ZFCW and FCW $M(T)$ increases with field for $\mu_0 H \geqslant 2$ T and
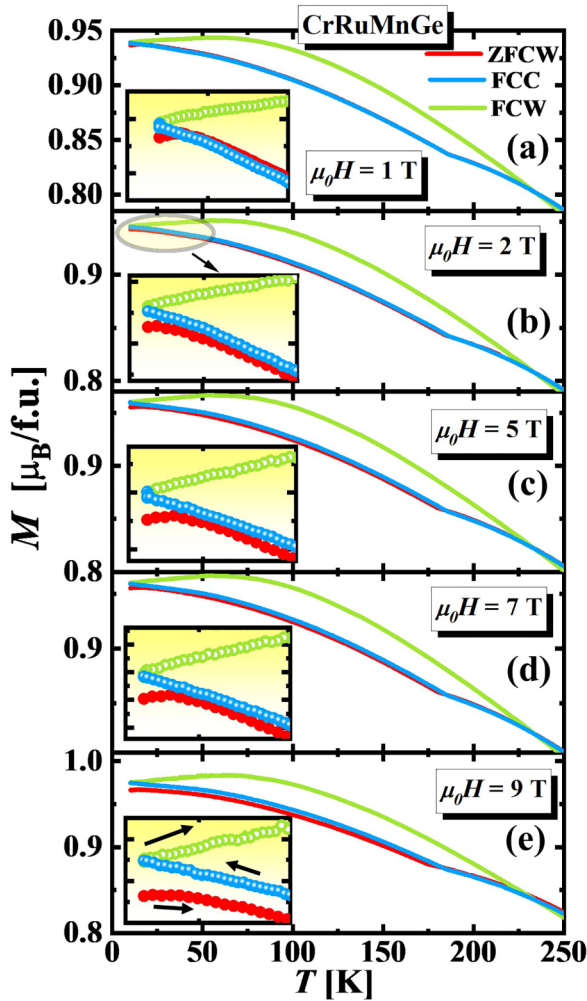
FIG. 4. ZFCW, FCC, and FCW $M(T)$ of the CrRuMnGe sample in the presence of an external magnetic field of (a) $\mu_0 H = 1$ T, (b) $\mu_0 H = 2$ T, (c) $\mu_0 H = 5$ T, (d) $\mu_0 H = 7$ T, and (e) $\mu_0 H = 9$ T. The insets show expanded views of the $M(T)$ curves in the temperature range $10\,\text{K} \leqslant T \leqslant 50\,\text{K}$.

becomes significant at the $\mu_0 H = 9$ T field, which is indicative of the fact that at high enough magnetic fields, the first-order austenite-martensitic phase transition is not completed but kinetically arrested [75]. It is also important to note that the abrupt drop in ZFCW $M(T)$ below 35 K is suppressed with increasing the magnetic field strength, indicating the occurrence of field induced metamagnetic transition from weak AFM to FM state at low temperatures.

Figure 2(d) exhibits the $M(H)$ loops at 300 and 10 K for the CrRuMnGe. Clearly, CrRuMnGe shows FM behavior with negligible magnetic hysteresis at both 300 and 10 K, indicating the soft ferromagnetic nature of this sample. Unlike the CrRuCoGe sample, the isothermal $M(H)$ curve shows complete saturation for the CrRuMnGe sample at 10 K which rules out the presence of the spin-glass-like magnetic ground state of this sample. However, as shown in the inset of Fig. 2(d), $M(H)$ of CrRuMnGe at 10 K demonstrates an interesting low field feature: a sharp magnetization switching near the zero field for both the forward and reverse branches of the $M(H)$ loop giving rise to a wasp-waist-shaped hysteresis loop. Such

a behavior has been observed in phase-segregated $Fe_{100-x}Gd_x$ alloy films [76], magnetically inhomogeneous C-deficient Mn_3GaC [77], the ternary shape memory alloy $Ni_{50}Mn_{34}In_{16}$ [75], etc. The wasp-waist-shaped $M(H)$ loop in the low field region for our CrRuMnGe alloy sample at low temperatures possibly arises due to field induced metamagnetic transition from the weak AFM to the FM state.

Another noteworthy feature of the $M(H)$ hysteresis loop for our CrRuMnGe alloy sample at 10 K is the appearance of the virgin curve outside the main $M(H)$ loop in the low field region, which supports the occurrence of kinetic arrest of the first-order austenite-martensitic phase transition in CrRuMnGe at low temperatures [75,78]. In other words, when the sample is zero field cooled from 300 to 10 K, the sample retains a certain phase fraction of the high temperature austenite phase which is in the metastable supercooled state and has a lower magnetization value compared to the martensitic counterpart [75], as shown in Figs. 3(c) and 3(d). After completing the initial virgin cycle, a majority of the metastable supercooled austenite phase fraction is converted into the equilibrium martensitic phase while reducing the field strength from the saturation magnetic field for both forward and reverse branches of the $M(H)$ loop, and leads to higher magnetization values in the subsequent field cycles than that in the initial virgin state [75]. The experimental value of saturation magnetization for the CrRuMnGe sample at 10 K is $M_S \approx 0.98\ \mu_B/\text{f.u.}$, which is very close to the M_S ($= 1\ \mu_B/\text{f.u.}$) value theoretically estimated using the Slater-Pauling rule [69], which further supports the absence of the glassy magnetic phase and, hence, the dominating FM phase at low temperatures [63].

To further probe the martensitic transformation in CrRuMnGe, temperature-dependent atomic force microscopy measurements were performed. Typical of bulk samples, the surface roughness is on the order of the topographical changes due to the characteristic twinning of the martensitic transformation. Figures 5(a) and 5(b) demonstrate larger scale scans at 300 and 190 K, respectively, which, due to the surface deformities, do not easily directly show twinning. However, a careful comparison of the 2D autocorrelation at 300 and 190 K [see Figs. 5(c) and 5(d), respectively] shows an elongation near the martensitic transformation temperature, which decreases as temperature is lowered from the transition temperature, resulting in a clear change in the angle between the twinning planes at the two temperatures [79,80]. The 2D autocorrelation allows for a statistical means of describing the degree of periodic surface topographical anisotropy, which is caused by the existence of twinning behavior. Figures 5(e) and 5(f) demonstrate a zoomed-in spot of an area [indicated by the red box in Figs. 5(a) and 5(b)] at 300 and 190 K, respectively, where a clear shift in twin boundaries is evident.

Figures 6(a) and 6(e) represent the temperature dependence of longitudinal electrical resistivity $\rho_{xx}(T)$ for CrRuCoGe and CrRuMnGe, respectively. Interestingly, while $\rho_{xx}(T)$ for CrRuCoGe shows semiconducting behavior ($\frac{\partial \rho_{xx}}{\partial T} < 0$) throughout the measured temperature range, that for CrRuMnGe exhibits metalliclike resistivity ($\frac{\partial \rho_{xx}}{\partial T} > 0$). A closer inspection reveals that the $\rho_{xx}(T)$'s for both CrRuCoGe and CrRuMnGe show a prominent slope change or point of inflection around $T = 100$ K. This slope change is more
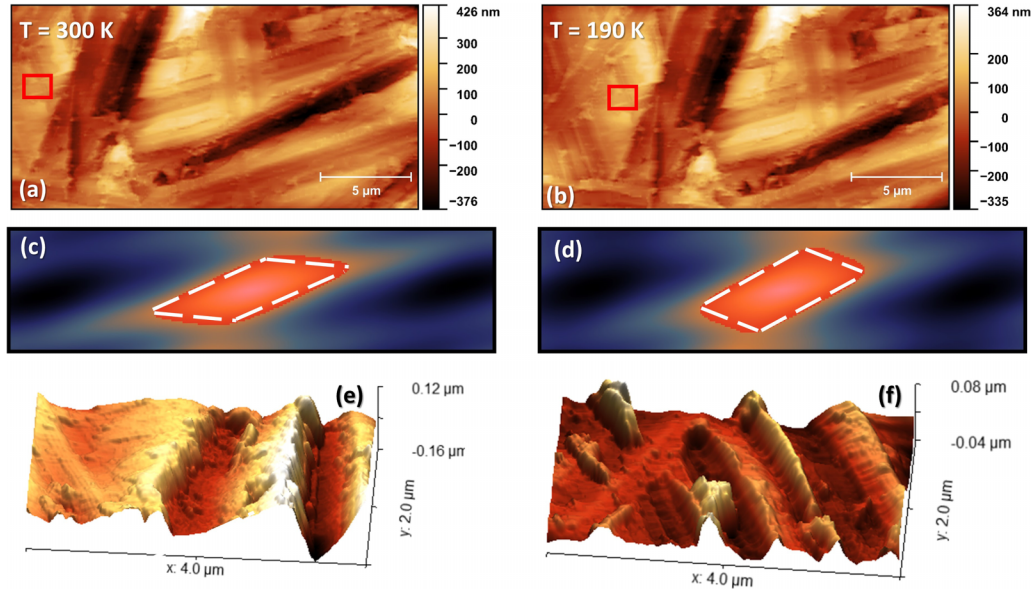
FIG. 5. Large scale atomic force microscopy scans for CrRuMnGe at (a) 300 K, and (b) 190 K. 2D autocorrelations for the same sample are shown at (c) 300 K, and (d) 190 K; (e), (f) demonstrate a zoomed-in spot of an area [indicated by red box in (a), (b)] at 300 and 190 K, respectively.

pronounced from the temperature-dependent $(\frac{d\rho_{xx}}{dT})$ curves shown in Figs. 6(a) and 6(e) for CrRuCoGe and CrRuMnGe, respectively, which show clear maxima at $T = 100$ K. Note that this point of inflection around $T = 100$ K does not correspond to martensitic transformation in the CrRuMnGe sample. More specifically, $\rho_{xx}(T)$ for the CrRuMnGe sample does not show any noticeable change around the martensitic transformation temperatures at $T_M = 180$ K and

$T_{MS} = 150$ K, which further confirms that the transformation is weaker compared to the conventional ferromagnetic shape memory alloy [72].

Next, we examine the longitudinal thermoelectric transport in these alloy samples. Figures 6(b) and 6(f) represent the T dependence of the longitudinal Seebeck coefficient $S_{xx}(T)$ for the CrRuCoGe and CrRuMnGe samples, respectively. Interestingly, while the sign of $S_{xx}(T)$ for the CrRuCoGe sample is negative throughout the measured temperature range, S_{xx} for the CrRuMnGe sample is positive, indicating that electrons (holes) are the dominating carriers for the thermally driven charge transport in CrRuCoGe (CrRuMnGe). We have analyzed the $S_{xx}(T)$ data for our samples considering different bulk scattering mechanisms which influence thermoelectric transport in a magnetic conductor/semiconductor. The diffusive component of S_{xx} for a three-dimensional (3D) semiconductor can be expressed as $S_{xx}^{3D}(T) = \frac{8\pi^2 m_d^* k_B^2 T}{3eh^2}(\frac{\pi}{N})^{2/3}$, where $N =$ carrier concentration, $k_B =$ Boltzmann constant, $e =$ electronic charge, $m_d^* =$ effective mass, and $h =$ Planck's constant [81]. It can be seen that $S_{xx}(T)$ for CrRuCoGe increases gradually with lowering the temperature down to ≈ 50 K, below which it shows a plateaulike behavior and then slowly approaches zero upon further lowering the temperature. Nevertheless, $S_{xx}(T)$ for CrRuMnGe also increases upon cooling from room temperature; however, it shows a prominent and broad maximum centered around 125 K, below which it decreases rapidly to zero upon further cooling. Note that the phonon-drag or magnon-drag effects can give rise to a maximum in $S_{xx}(T)$ at low temperatures [82,83]. The contribution of phonon-drag effect (S_{ph}) toward S_{xx} varies as T^3 [82,83], whereas the contribution of magnon-drag effect (S_{mag}) typically shows $T^{3/2}$ dependence [82,84]. Considering the aforementioned scattering mechanisms, we fitted our $S_{xx}(T)$ data for the CrRuCoGe and
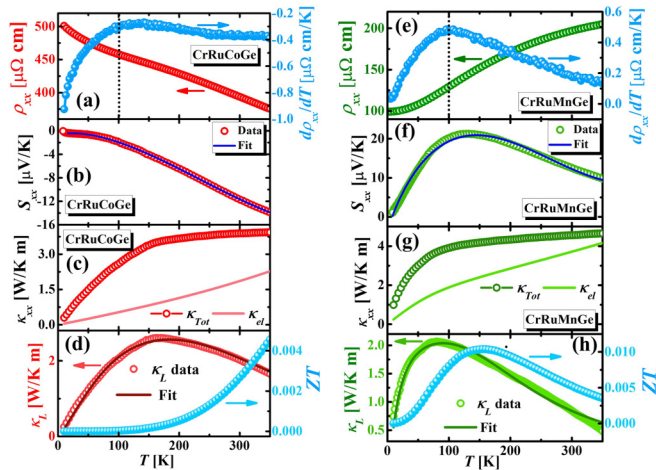

FIG. 6. Temperature dependence of longitudinal resistivity $\rho_{xx}(T)$ for (a) CrRuCoGe, and (e) CrRuMnGe on the left y scales. The temperature-dependent $(\frac{d\rho_{xx}}{dT})$ curves for these samples are shown on the right y scales. Temperature dependence of S_{xx} for (b) CrRuCoGe, and (f) CrRuMnGe. Temperature dependence of κ_{xx}^{Tot} and κ_{xx}^{el} for (c) CrRuCoGe, and (g) CrRuMnGe. Temperature dependence of κ_{xx}^{L} fitted with Callaway's model (left y scales) for (d) CrRuCoGe, and (h) CrRuMnGe; right y scales show temperature dependence of thermoelectric figure of merit ZT.

CrRuMnGe samples using the expression [84,85]: $S_{xx}(T) = S_0 + S_{xx}^{3D}T + S_{mag}T^{3/2} + S_{ph}T^3 + S_{SW}T^4$, where the fifth term accounts for contributions from spin-wave fluctuations. From the fits we obtained, $S_0 = -0.70 \pm 0.03$ μV/K, $S_{xx}^{3D} = 0.036 \pm 0.002$ μV/K^{-2}, $S_{mag} = (-5.0 \pm 0.2) \times 10^{-3}$ μV/K$^{-5/2}$, $S_{ph} = (1.3 \pm 0.3) \times 10^{-7}$ μV/K^{-4}, and $S_{SW} = (10 \pm 5) \times 10^{-10}$ μV/K^{-5} for CrRuCoGe; and $S_0 = -3.6 \pm 0.2$ μV/K, $S_{xx}^{3D} = 0.57 \pm 0.01$ μV/K^{-2}, $S_{mag} = (-3.4 \pm 0.1) \times 10^{-2}$ μV/K$^{-5/2}$, $S_{ph} = (8.9 \pm 0.2) \times 10^{-7}$ μV/K^{-4}, and $S_{SW} = (2.3 \pm 1) \times 10^{-10}$ μV/K^{-5} for CrRuMnGe. Clearly, the absolute values of S_{mag} are approximately four and five orders of magnitude higher than those of S_{ph} for CrRuCoGe and CrRuMnGe, respectively, indicating dominant contribution of the magnon-drag effect in both samples. Notably, the phonon-drag effect induced maximum in $S_{xx}(T)$ usually occurs around $T \approx (\theta_D/5)$ [83], where θ_D is the Debye temperature. The values of θ_D for CrRuCoGe and CrRuMnGe are found to be $\approx$490 and 252 K, respectively. Therefore, the phonon-drag-driven maximum in $S_{xx}(T)$ is expected to occur $\approx$98 K for CrRuCoGe and $\approx$50 K for CrRuMnGe. However, $S_{xx}(T)$ for CrRuCoGe shows a plateaulike behavior around 50 K and that for CrRuMnGe shows a maximum around 125 K, indicating that the magnon-drag effect is primarily responsible for the behavior of $S_{xx}(T)$ for both samples. Furthermore, $|S_{mag}|$ for CrRuMnGe is one order of magnitude higher than that of CrRuCoGe, which is consistent with the fact that $S_{xx}(T)$ for CrRuMnGe shows a more prominent maximum in comparison to the weak plateaulike behavior in CrRuCoGe.

Figures 6(c) and 6(g) show the temperature dependence of total longitudinal thermal conductivity, $\kappa_{xx}^{Tot}(T)$ in the temperature range 5 K $\leqslant T \leqslant$ 350 K for CrRuCoGe and CrRuMnGe, respectively. Using $\rho_{xx}(T)$, we have estimated the temperature dependence of the electronic thermal conductivity, $\kappa_{xx}^{el}(T)$ from the Wiedemann-Franz law: $\kappa_{xx}^{el} = \frac{L_0 T}{\rho_{xx}}$, where $L_0 = \frac{\pi^2 k_B^2}{3e^2} = 2.44 \times 10^{-8}$ WΩK^{-1} is the Lorenz number for free electrons [86]. The solid lines in Figs. 6(c) and 6(g) demonstrate $\kappa_{xx}^{el}(T)$ for CrRuCoGe and CrRuMnGe, respectively. Magnons in a magnetically ordered system can also contribute toward the total thermal conductivity. In general, the magnonic contribution is $\approx$5%−10% of κ_{xx}^{Tot} around T_C in most of the magnetic conductors/semiconductors [87]. Since the magnetic ordering temperature for both CrRuCoGe and CrRuMnGe samples is well above 300 K, we have considered only the lattice and electronic contributions toward κ_{xx}^{Tot} for both our samples. The left y scales of Figs. 6(d) and 6(h) exhibit the temperature dependence of the lattice thermal conductivity, $\kappa_{xx}^{L}(T)$ for CrRuCoGe and CrRuMnGe, respectively, estimated using the expression $\kappa_{xx}^{L}(T) = [\kappa_{xx}^{Tot}(T) - \kappa_{xx}^{el}(T)]$. While $\kappa_{xx}^{L}(T)$ for CrRuCoGe shows a maximum around $\approx$150 K, that for CrRuMnGe exhibits a comparatively sharper maximum around $\approx$75 K. To have a clearer understanding about the contributions of different phonon scattering mechanisms toward the lattice thermal conductivity, we fitted $\kappa_{xx}^{L}(T)$ for CrRuCoGe and CrRuMnGe with the Debye-Callaway model [88,89],

$$\kappa_{xx}^{L}(T) = \frac{k_B}{2\pi^2 v_S}\left(\frac{2\pi k_B T}{h}\right)^3 \int_0^{(\theta_D/T)} \frac{\tau_L z^4 e^z}{(e^z-1)^2}dz. \quad (1)$$

Here, v_S is the average phonon velocity, $z = frac\hbar\omega k_B T$, ω = phonon frequency, and τ_L is the total phonon relaxation time. Here, τ_L can be expressed as a linear combination of different phonon scattering mechanisms as $\tau_L^{-1} = \tau_B^{-1} + \tau_D^{-1} + \tau_U^{-1} + \tau_{e-Ph}^{-1}$, where τ_B^{-1}, τ_D^{-1}, τ_U^{-1}, and τ_{e-Ph}^{-1} signify the reciprocal of the relaxation times associated with phonon-boundary scattering, phonon scattering by point defects, the umklapp scattering process, and the electron-phonon scattering, respectively [90]. In the case of the diffusive boundary scattering, $\tau_B^{-1} = \frac{v_S}{D}$, where $D_{Ph} = \delta\lambda_{Ph}$ is the effective mean free path, λ_{Ph} = mean free path of phonons, and δ is the correction factor related to the phonon scattering at the grain boundary. For a polycrystalline sample, $\lambda_{Ph} \approx$ the average grain size. In the case of scattering of phonons by point defects, $\tau_D^{-1} = A\omega^4$, where the parameter A depends on the mass-fluctuation scattering and phonon speed [91]. For the umklapp scattering process [92], $\tau_U^{-1} = B\omega^2 T e^{-(\theta_D/T)}$, where B is a fitting parameter, and for the electron-phonon scattering process, $\tau_{e-Ph}^{-1} = C\omega^2$ [93]. We have considered $v_S = 4 \times 10^3$ m s^{-1} for both CrRuCoGe and CrRuMnGe, which is close to the average phonon velocity reported for the semimetallic Heusler alloy CoFeVSb [25]. As shown from our XRD analysis, the average grain sizes for CrRuCoGe and CrRuMnGe are $\approx$23 and 41 nm, respectively. Best fits were obtained for $\delta = 12.5$ and 15 which correspond to $D_{Ph} \approx 0.28 \times 10^{-6}$ m and $\approx 0.62 \times 10^{-6}$ m for CrRuCoGe and CrRuMnGe, respectively. The values of the fitting parameters for CrRuCoGe are $A = (5.5 \pm 0.5) \times 10^{-43}$ s^3, $B = (9.8 \pm 0.4) \times 10^{-23}$ s K^{-1}, $C = (2.8 \pm 0.1) \times 10^{-15}$ s, and $\theta_D = (490 \pm 5)$ K, respectively. For CrRuMnGe, the values of the fitting parameters are $A = (2.5 \pm 0.2) \times 10^{-41}$ s^3, $B = (1.9 \pm 0.1) x \times 10^{-22}$ s K^{-1}, $C = (1.55 \pm 0.06) \times 10^{-17}$ s, and $\theta_D = (252 \pm 3)$ K, respectively. Clearly, contributions of the point defect scattering and the umklapp scattering toward lattice thermal transport are higher in CrRuMnGe than in CrRuCoGe, whereas the contribution of electron-phonon scattering plays a dominating role in CrRuCoGe in contrast to CrRuMnGe. Most importantly, θ_D of CrRuCoGe is almost two times higher than that of CrRuMnGe. Furthermore, the thermoelectric figure of merit, $ZT = \frac{S_{xx}^2}{\kappa_{xx}^{Tot}\rho_{xx}}T$ [94], of CrRuCoGe is $\approx$0.0045 at 350 K, while that of CrRuMnGe is 0.0034. However, ZT of CrRuCoGe decreases gradually with decreasing temperature, whereas that of CrRuMnGe increases with decreasing temperature and shows a maximum value of $\approx$0.01 at 150 K and then decreases swiftly with further decreasing temperature [see right y scales of Figs. 6(d) and 6(h), respectively].

Next, we discuss the transverse thermoelectric properties of CrRuCoGe and CrRuMnGe. Figure 7(a) displays the schematic illustration of the experimental configuration of ANE measurements on the samples under consideration [95]. The sample was sandwiched between two copper blocks and a temperature gradient was applied along the z direction (along the thickness of the sample) as a result of which, the temperature difference generated between the bottom (hot) and top (cold) copper blocks is given by $\Delta T = (T_{hot} - T_{cold})$. In the presence of a temperature gradient along the z direction, and the application of an external magnetic field along the x direction, a transverse anomalous Nernst voltage is generated along the y direction. Figures 7(b) and 7(c) show the magnetic
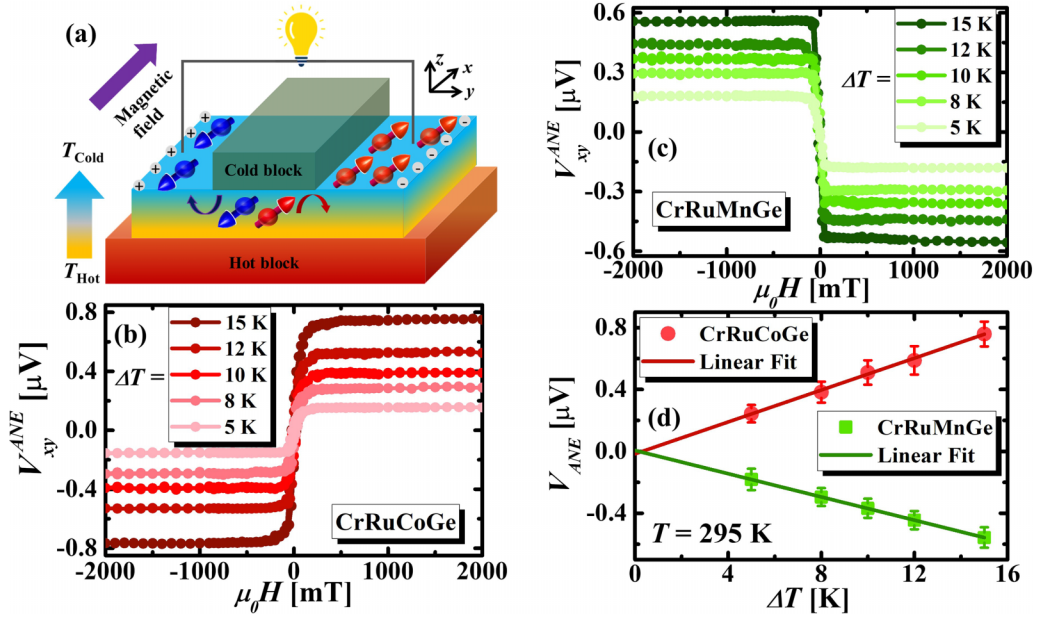
FIG. 7. (a) Schematic illustration of Nernst measurement. Magnetic field dependence of anomalous Nernst voltage $V_{xy}^{ANE}(H)$ for different values of ΔT at $T = 295$ K for (b) CrRuCoGe, and (c) CrRuMnGe. (d) The background corrected anomalous Nernst voltage, $V_{ANE}(\mu_0 H_{sat}) = [\frac{V_{xy}^{ANE}(+\mu_0 H_{sat}) - V_{xy}^{ANE}(-\mu_0 H_{sat})}{2}]$ as a function of ΔT.

field dependence of the anomalous Nernst voltage, $V_{xy}^{ANE}(H)$ for different values of ΔT for CrRuCoGe and CrRuMnGe samples, respectively, at a fixed average sample temperature $T = \frac{T_{hot} + T_{cold}}{2} = 295$ K. While the isothermal $V_{xy}^{ANE}(H)$ loops show small hysteresis for CrRuCoGe, that for CrRuMnGe shows negligible hysteresis, both mimicking their respective $M(H)$ behavior. Furthermore, the $V_{xy}^{ANE}(H)$ signal strength increases with increasing ΔT, which is quite obvious as the transverse electric voltage (V_{ANE}) generated due to ANE can be expressed as $V_{ANE} = S_{ANE}|\mu_0 \vec{M} \times \overrightarrow{\nabla T}|$, where $\overrightarrow{\nabla T}$ is the applied temperature gradient, $\vec{M}$ is the magnetization of the sample, and S_{ANE} is the anomalous Nernst coefficient [6,29]. Figure 7(d) displays the background corrected anomalous Nernst voltage, $V_{ANE}(\mu_0 H_{sat}) = [\frac{V_{xy}^{ANE}(+\mu_0 H_{sat}) - V_{xy}^{ANE}(-\mu_0 H_{sat})}{2}]$ as a function of ΔT for the samples CrRuCoGe and CrRuMnGe, respectively, at $T = 295$ K, where $\mu_0 H_{sat}$ is the saturation field. Evidently, $V_{ANE}(\mu_0 H_{sat})$ varies linearly with ΔT for both samples, indicating intrinsic contribution of the thermally generated ANE [10,14]. Most importantly, the sign of $V_{ANE}(\mu_0 H_{sat})$ for CrRuMnGe is opposite to that of Cr-RuCoGe; i.e., CrRuCoGe shows positive ANE, whereas CrRuMnGe exhibits negative ANE. The negative sign of ANE has been observed in Mn-based ordered alloys, e.g., epitaxial thin films of $Mn_x Ga_{100-x}$, [51] $L1_0$ ordered MnGa [52] and $D0_{22}$-ordered Mn_2Ga thin films, [53] polycrystalline MnBi [54], etc., and this has been discussed in terms of the competition between transverse thermoelectric conduction and the anomalous Hall effect (AHE) acting on the thermally generated carrier flow induced by the longitudinal Seebeck effect [51]. We will discuss the possible origin of the negative sign of ANE in our CrRuMnGe alloy briefly in the following section.

In Figs. 8(a) and 8(c), we demonstrate the $V_{xy}^{ANE}(H)$ hysteresis loops for the samples CrRuCoGe and CrRuMnGe,

respectively, at selected temperatures in the range 140 K $\leqslant T \leqslant 295$ K for fixed $\Delta T = +15$ K. For CrRuCoGe, $V_{xy}^{ANE}(H)$ signal strength clearly decreases with decreasing temperature. The $V_{xy}^{ANE}(H)$ signal strength for CrRuMnGe also decreases with reducing temperature; however, the change in $|V_{xy}^{ANE}(\mu_0 H_{sat})|$ with respect to temperature is small in comparison to that of the CrRuCoGe sample. Furthermore, the sign of V_{xy}^{ANE} remains positive for CrRuCoGe and negative for CrRuMnGe throughout the measured temperature range. The left y scales of Figs. 9(a) and 9(d) demonstrate the temperature dependence of the background-corrected anomalous Nernst coefficient [10,14], $S_{ANE}(\mu_0 H_{sat}, T) = \frac{V_{ANE}(\mu_0 H_{sat}, T)}{\Delta T_{eff}}(\frac{L_z}{L_y}) = \frac{1}{2}\frac{[V_{xy}^{ANE}(+\mu_0 H_{sat}, T) - V_{xy}^{ANE}(-\mu_0 H_{sat}, T)]}{\Delta T_{eff}}(\frac{L_z}{L_y})$ for the samples CrRuCoGe and CrRuMnGe, respectively, where $L_y (\approx 3$ mm) is the distance between the voltage leads for the ANE measurements and L_z (≈ 2 mm for CrRuCoGe and ≈ 1.75 mm for CrRuMnGe) is the thickness of the samples, and ΔT_{eff} is the effective temperature difference across the sample. Considering the drop in temperature gradient in the N grease layers on both sides of the sample, and neglecting the interfacial thermal resistances between the hot/cold copper blocks and the N grease layers as well as the interfacial thermal resistances between the sample surfaces and the N grease layers, ΔT_{eff} can be written as [13,25,96] $\Delta T_{eff} = \frac{\Delta T}{[1+(\frac{2L_{N Grease}}{\kappa_{N Grease}})(\frac{\kappa_{CrRuXGe}}{L_{CrRuXGe}})]}$. Here, $L_{N Grease}$ and $\kappa_{N Grease}$ are the thickness and thermal conductivity of the N grease layer; $L_{CrRuXGe}$ and $\kappa_{CrRuXGe}$ are the thickness and thermal conductivity of the CrRuXGe samples ($X =$ Co, Mn). Using the previously reported values of the temperature dependence of $\kappa_{N Grease}$ of N grease [97], and considering, $L_{N Grease} \approx 10$ µm, $L_{CrRuXGe} \approx 2$ mm for CrRuCoGe and ≈ 1.75 mm for CrRuMnGe, we estimated the temperature
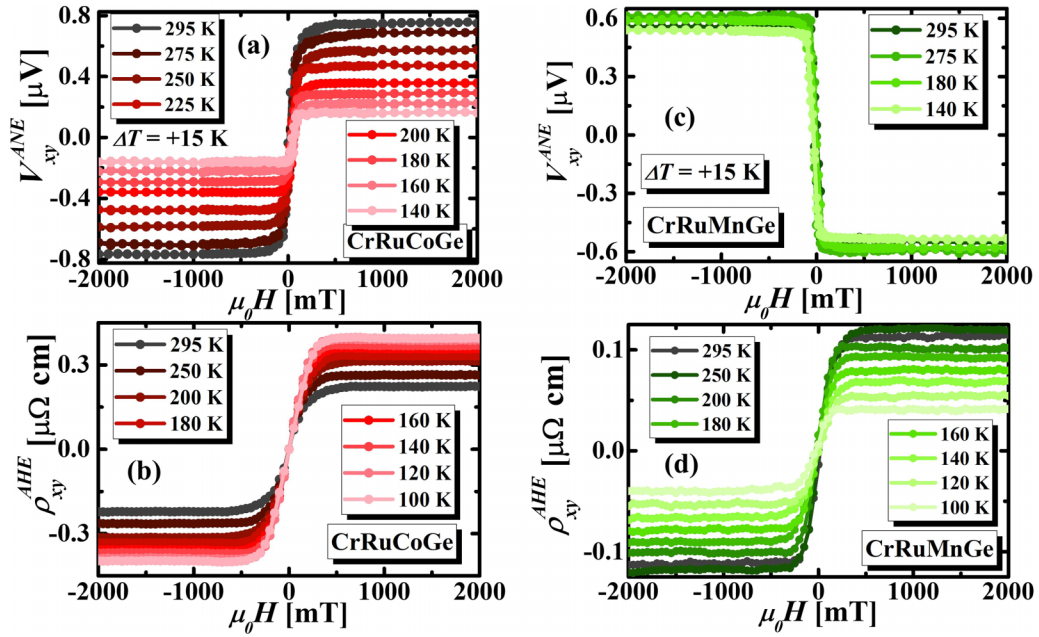
FIG. 8. $V_{xy}^{ANE}(H)$ hysteresis loops for the samples (a) CrRuCoGe, and (c) CrRuMnGe, respectively, at selected temperatures in the range $140\,\text{K} \leqslant T \leqslant 295\,\text{K}$ for fixed $\Delta T = +15\,\text{K}$. Magnetic field dependence of anomalous Hall resistivity $\rho_{xy}^{AHE}(H)$ for (b) CrRuCoGe, and (d) CrRuMnGe, respectively, at selected temperatures in the range $100\,\text{K} \leqslant T \leqslant 295\,\text{K}$.

dependence of ΔT_{eff}, which we have used to determine $S_{ANE}(\mu_0 H_{\text{sat}}, T)$. The estimated value of S_{ANE} for CrRuCoGe at $T = 295\,\text{K}$ is $(58 \pm 0.5)\,\text{nV K}^{-1}$ which is larger than that for $\text{Ni}_{81}\text{Fe}_{19} \approx 48\,\text{nV K}^{-1}$ [98], and compressively strained SrRuO_3 films $(\approx 30\,\text{nV K}^{-1})$ [99]. On the other

hand, the value of $|S_{ANE}|$ for CrRuMnGe at 295 K is lower $(\approx 40.0 \pm 0.2\,\text{nV K}^{-1})$ than that of CrRuCoGe, but comparable to that of the semimetallic Heusler alloy CoFeVSb $(\approx 39\,\text{nV K}^{-1})$ [25] and larger than the spin-gapless semiconductor CoFeCrGa $(\approx 18\,\text{nV K}^{-1})$ [13]. As seen
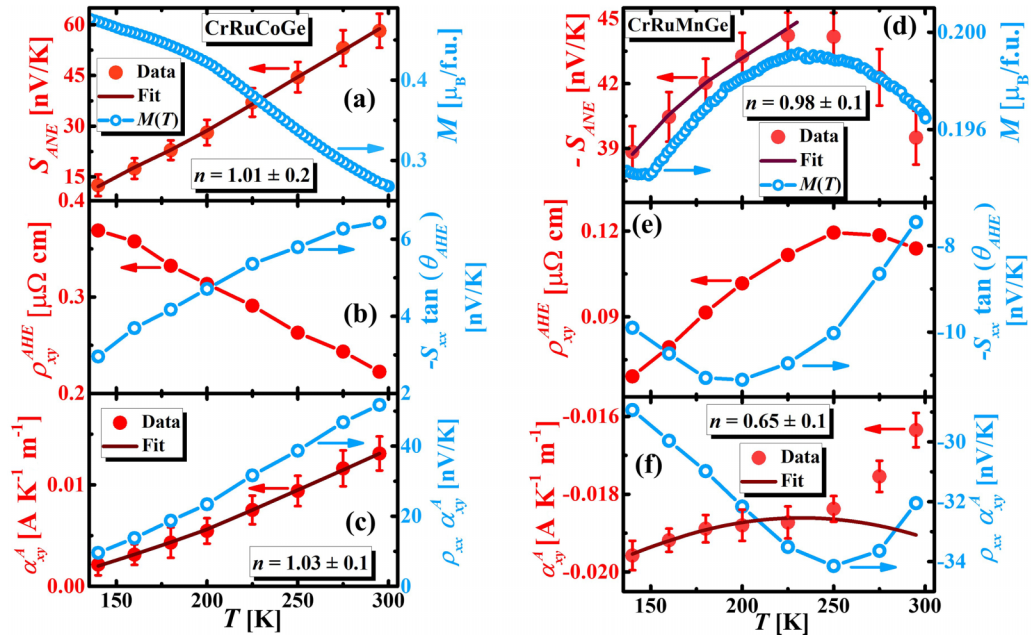

FIG. 9. Temperature dependence of the background-corrected anomalous Nernst coefficient, $S_{ANE}(\mu_0 H_{\text{sat}}, T) = \frac{V_{ANE}(\mu_0 H_{\text{sat}}, T)}{\Delta T_{\text{eff}}}\left(\frac{L_z}{L_y}\right)$ for (a) CrRuCoGe, and (b) CrRuMnGe, respectively, are shown on the left y scales; the right y scales show the corresponding FC $M(T)$ of these samples. The left y scales of (b), (e) demonstrate the temperature dependence of anomalous Hall resistivity $\rho_{xy}^{AHE}(\mu_0 H_{\text{sat}}, T)$ for CrRuCoGe and CrRuMnGe, respectively, and the right y scales show the corresponding temperature dependence of $-S_{xx}\tan(\theta_{AHE})$. The left y scales of (c), (f) show $\alpha_{xy}^A(T)$ for the CrRuCoGe and CrRuMnGe samples, respectively, and the right y scales demonstrate the corresponding temperature dependence of $\rho_{xx}\alpha_{xy}^A$.

in Figs. 9(a) and 9(d), $|S_{ANE}(\mu_0 H_{sat}, T)|$ for CrRuCoGe decreases monotonically with decreasing temperature, whereas that for CrRuMnGe first increases with decreasing temperature from 295 K and shows a broad maximum around 225 K, followed by a gradual decrease upon further lowering the temperature.

Now let us understand the origins of $S_{ANE}(\mu_0 H_{sat}, T)$ in the CrRuCoGe and CrRuMnGe alloys. In general, S_{ANE} can be decomposed into two terms as [6,51,100] $S_{ANE} = (\rho_{xx}\alpha_{xy}^A - \rho_{xy}^{AHE}\alpha_{xx})$, where α_{xy}^A is the anomalous transverse thermoelectric conductivity, ρ_{xy}^{AHE} is the anomalous Hall resistivity, and α_{xx} is the longitudinal thermoelectric conductivity. According to the Mott's relations, $\alpha_{xy}^A = \frac{\pi^2 k_B^2 T}{3e}(\frac{\partial \sigma_{xy}^{AHE}}{\partial E})_{E=E_F}$ and $\alpha_{xx} = \frac{\pi^2 k_B^2 T}{3e}(\frac{\partial \sigma_{xx}}{\partial E})_{E=E_F}$, where E_F is the Fermi energy [6,101]. Here, the anomalous Hall conductivity σ_{xy}^{AHE} and longitudinal electrical conductivity σ_{xx} can be expressed as [6,18,27] $|\sigma_{xy}^{AHE}| = [\frac{\rho_{xy}^{AHE}}{(\rho_{xx})^2 + (\rho_{xy}^{AHE})^2}]$ and $|\sigma_{xx}| = [\frac{\rho_{xx}}{(\rho_{xx})^2 + (\rho_{xy}^{AHE})^2}]$, respectively. According to the power law for AHE, $\rho_{xy}^{AHE} = \lambda \rho_{xx}^n$, where λ is the spin-orbit coupling constant and n is an exponent. Considering all the aforementioned expressions, $S_{ANE}(T)$ can be written as [6,14]

$$S_{ANE}(T) = \rho_{xx}^{n-1}\left[\frac{\pi^2 k_B^2 T}{3e}\left(\frac{\partial \lambda}{\partial E}\right)_{E=E_F} - (n-1)\lambda S_{xx}\right]. \quad (2)$$

It is known that the extrinsic skew scattering is the dominant mechanism for the anomalous Nernst/Hall transport for $n = 1$, and the intrinsic Berry curvature or the side jump is the dominating mechanism for $n = 2$ [31]. We fitted the $S_{ANE}(\mu_0 H_{sat}, T)$ data for CrRuCoGe and $-S_{ANE}(\mu_0 H_{sat}, T)$ data for CrRuMnGe within the measured temperature range (for the CrRuMnGe, the fitting was done in the temperature range 140 K $\leqslant T \leqslant$ 225 K) using Eq. (2) and considering λ, $(\frac{\partial \lambda}{\partial E})_{E=E_F}$, and n as the fitting parameter. We found that the best fits were obtained for $n = (1.01 \pm 0.20)$ and $n = (0.98 \pm 0.10)$ for CrRuCoGe and CrRuMnGe, respectively, signifying that the origin of ANE in both of these samples is dominated by the asymmetric skew scattering of charge carriers in the measured temperature regime [13,31]. Similar to CrRuMnGe, extrinsic skew scattering dominated large ANE has also been observed across the martensitic phase transition in the $Ni_{46.5}Co_2Mn_{37}Sn_{14.5}$ Heusler alloy [44]. To further shed light on the origins of the observed ANE, it is convenient to analyze $\alpha_{xy}^A(T)$, which can be written as [23,24,102] $\alpha_{xy}^A = S_{ANE}\sigma_{xx} + S_{xx}\sigma_{xy}^{AHE}$. According to the Mott's relations, α_{xy}^A can be expressed as [6,14]

$$\alpha_{xy}^A = rho_{xx}^{n-2}\left[\frac{\pi^2 k_B^2 T}{3e}\left(\frac{\partial \lambda}{\partial E}\right)_{E=E_F} - (n-2)\lambda S_{xx}\right]. \quad (3)$$

We have performed AHE measurements on both the CrRuCoGe and CrRuMnGe samples to determine $\alpha_{xy}^A(T)$. Figures 8(b) and 8(d) demonstrate the magnetic field dependence of anomalous Hall resistivity $\rho_{xy}^{AHE}(H)$ for CrRuCoGe and CrRuMnGe, respectively, at selected temperatures in the range 100 K $\leqslant T \leqslant$ 295 K. Clearly $\rho_{xy}^{AHE}(H)$ for CrRuCoGe increases with decreasing temperature, whereas

that for CrRuMnGe decreases with a decrease in temperature. The left y scales of Figs. 9(b) and 9(e) demonstrate the temperature dependence of anomalous Hall resistivity, $\rho_{xy}^{AHE}(\mu_0 H_{sat}, T)$, for CrRuCoGe and CrRuMnGe, respectively. For both samples, the trend of $\rho_{xy}^{AHE}(\mu_0 H_{sat}, T)$ is opposite to that of $S_{ANE}(\mu_0 H_{sat}, T)$, but identical to that of $M(T)$. More specifically, $\rho_{xy}^{AHE}(\mu_0 H_{sat}, T)$ for CrRuCoGe increases monotonically with decreasing temperature, whereas that for CrRuMnGe shows a maximum around 250 K and then decreases monotonically with further lowering of the temperature, similar to the trend of $-S_{ANE}(\mu_0 H_{sat}, T)$. Significant changes in the anomalous Hall conductivity in the vicinity of martensitic transition is reported in the magnetic shape memory alloy Ni_2MnGa [103]. As shown on the left y scales of Figs. 9(c) and 9(f), $\alpha_{xy}^A(T)$ for CrRuCoGe is positive throughout the measured temperature range and shows a nearly linear decrease with decreasing temperature, whereas that for CrRuMnGe is negative throughout the measured temperature range and shows nonmonotonic decrease with decreasing temperature. We fitted $\alpha_{xy}^A(T)$ for both CrRuCoGe and CrRuMnGe using Eq. (3), and the best fits were acquired for $n = (1.03 \pm 0.3)$ and $n = (0.65 \pm 0.1)$, respectively, which are close to those obtained by fitting the $S_{ANE}(\mu_0 H_{sat}, T)$ data and, hence, further confirm that the observed ANE in these samples is governed by the extrinsic skew scattering mechanism [31]. It is noteworthy that the longitudinal electrical conductivity, $\sigma_{xx} = [\frac{\rho_{xx}}{(\rho_{xx})^2 + (\rho_{xy}^{AHE})^2}]$ for CrRuCoGe and CrRuMnGe was found to be in the ranges of $\sigma_{xx} \approx 2 \times 10^3 - 2.5 \times 10^3$ S cm^{-1} and $\sigma_{xx} \approx 5 \times 10^3 - 6 \times 10^3$ S cm^{-1}, respectively, in the measured temperature regime, both of which are nearly one order of magnitude lower than the moderate conductivity range of $10^4 \leqslant \sigma x^{xx} \leqslant 10^6$ S cm^{-1}, where the intrinsic contribution of AHE and, hence, ANE is expected [103]. Therefore, for both CrRuCoGe and CrRuMnGe, the dominant role of extrinsic skew scattering toward the anomalous Hall and Nernst transports is expected in the measured temperature regime.

It is interesting to note that $-S_{ANE}(\mu_0 H_{sat}, T)$ for CrRuMnGe follows the FCW $M(T)$ curve [as seen in Fig. 9(d)], indicating that the martensitic transformation influences the ANE signal. Large changes in the anomalous Nernst coefficient across the magnetostructural transition are reported in Mn-based full Heusler alloys: Ni_2MnGa and $Ni_{46.5}Co_2Mn_{37}Sn_{14.5}$ [16,44]. Since $\alpha_{xy}^A = \frac{\pi^2 k_B^2 T}{3e}(\frac{\partial \sigma_{xy}^{AHE}}{\partial E})_{E=E_F}$ and S_{ANE} is directly related to α_{xy}^A, both these quantities are susceptible to the changes in the Fermi surface. Therefore, during the cubic to tetragonal transformation, the competition between the surface energy associated with the boundary between two orientational variants of the tetragonal martensitic phase and the elastic energy related to lattice mismatch leads to the formation of an elastically strained phase known as the adaptive martensitic phase which causes a significant change in the Fermi surface [80]. Since $S_{xx} \propto (\frac{\partial \ln\{\sigma_{xx}(E)\}}{\partial E})_{E=E_F}$, and $\sigma_{xx}(E)$ is proportional to the density of states, the temperature-dependent S_{xx} should also exhibit significant change around the martensitic transformation [16]. However, unlike $S_{ANE}(T)$, $S_{xx}(T)$ for our CrRuMnGe alloy does not show any noticeable change around the martensitic transformation temperature. Such discrepancy can be associ-

ated with the difference in measurement protocol between the longitudinal thermopower and transverse ANE [16]. While $S_{xx}(T)$ was measured in the absence of an external magnetic field, ANE was measured in the presence of an external magnetic field. Application of the external magnetic field gives rise to magnetic field induced strain, which also causes significant changes in the Fermi surface. Therefore, the prominent maximum in $-S_{ANE}(\mu_0 H_{sat}, T)$ in the vicinity of the martensitic transformation temperature is related to the magnetic field induced strain and related changes in the Fermi surface [16]. Since the martensitic transformation in CrRuMnGe is much weaker than that observed in the aforementioned full Heusler alloys [16,44], the change in $|S_{ANE}(\mu_0 H_{sat}, T)|$ with temperature is relatively smaller for CrRuMnGe.

Next, let us discuss the opposite signs of $S_{ANE}(\mu_0 H_{sat}, T)$ in CrRuCoGe and CrRuMnGe. We recall that S_{ANE} can be considered as a linear combination of two terms as [15,51,104] $S_{ANE} = S_1^{ANE} + S_2^{ANE} = (\rho_{xx}\alpha_{xy}^A - \rho_{xy}^{AHE}\alpha_{xx})$. Here, the first term $S_1^{ANE} = \rho_{xx}\alpha_{xy}^A$ arises from the transverse thermoelectric conduction that directly transforms the thermal gradient $\overrightarrow{\nabla T}$ into transverse electric current, $\overrightarrow{J_y^A} = \alpha_{xy}^A \overrightarrow{\nabla T}$ [51]. On the other hand, the second term, $S_2^{ANE} = -\rho_{xy}^{AHE}\alpha_{xx}$, represents the contribution of AHE acting on the thermally generated carrier flow induced by the longitudinal Seebeck effect [51]. Here, S_2^{ANE} can be rewritten as [51] $S_2^{ANE} = -\rho_{xy}^{AHE}\alpha_{xx} = -S_{xx}(\frac{\rho_{xy}^{AHE}}{\rho_{xx}}) = -S_{xx}\tan(\theta_{AHE})$, where $\tan(\theta_{AHE}) = (\frac{\rho_{xy}^{AHE}}{\rho_{xx}})$ is the anomalous Hall angle. Therefore, the sign of the resultant ANE would be determined by these two competing contributions. The right y scales of Figs. 9(b) and 9(e) show the temperature dependence of $-S_{xx}\tan(\theta_{AHE})$, and the right y scales of Figs. 9(c) and 9(f) demonstrate the temperature dependence of $\rho_{xx}\alpha_{xy}^A$, for Cr-RuCoGe and CrRuMnGe, respectively. Clearly, both $\rho_{xx}\alpha_{xy}^A$ and $-S_{xx}\tan(\theta_{AHE})$ are positive for CrRuCoGe throughout the measured temperature range, which explains the positive sign of ANE for this sample. On the contrary, both $\rho_{xx}\alpha_{xy}^A$ and $-S_{xx}\tan(\theta_{AHE})$ for CrRuMnGe are negative throughout the measured temperature regime, which explains the observed negative sign of $S_{ANE}(\mu_0 H_{sat}, T)$ for this sample [51]. Furthermore, $|S_{xx}\tan(\theta_{AHE})| \ll |\rho_{xx}\alpha_{xy}^A|$ for both alloys throughout the measured temperature range, as observed in Mn-Ga ordered alloys [51]. However, this observation is in sharp contrast to the Mn-based (Mn-Cr)AlGe alloy film, for which $|S_{xx}\tan(\theta_{AHE})| \gg |\rho_{xx}\alpha_{xy}^A|$ and the negative sign of S_{ANE} in this material is predominantly caused by the large positive value of S_{xx} in combination with the negative sign of α_{xy}^A [55]. On the other hand, in the case of both the CrRuMnGe and CrRuCoGe alloys, the contribution of the anomalous transverse thermoelectric conduction α_{xy}^A dominates that of the AHE acting on the thermally generated carrier flow induced by the longitudinal Seebeck effect [51]. Therefore, the sign of S_{ANE} in both CrRuMnGe and Cr-RuCoGe samples is determined by the sign of α_{xy}^A. Since α_{xy}^A is positive for CrRuCoGe but negative for CrRuMnGe, the sign of S_{ANE} is also positive for CrRuCoGe and negative for CrRuMnGe in the measured temperature range. It is also noteworthy that the bipolarity of S_{ANE} in the topological Weyl
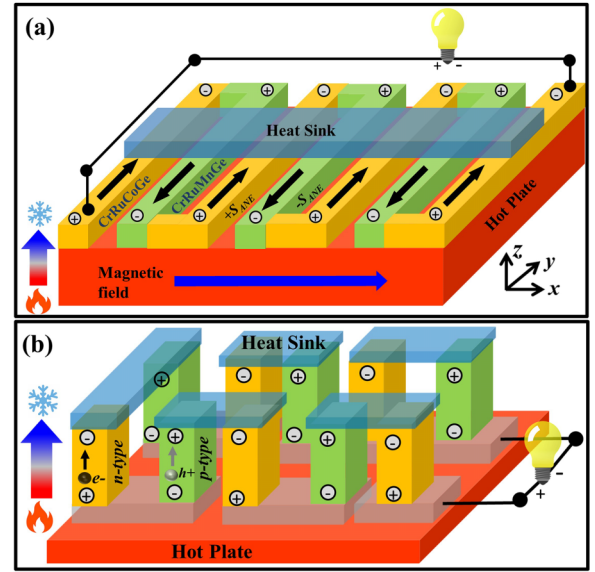

FIG. 10. (a) Proposed prototype of the ANE-based thermopile device configuration using the Heusler alloys CrRuXGe (X = Mn, Co) at room temperature. (b) Schematic illustration of a conventional longitudinal Seebeck-based thermopile device with assemblies of coupled p- and n-type legs.

ferromagnet $Co_3Sn_2S_2$ is associated with the intrinsic Berry curvature contribution [49], whereas the sign tunability of S_{ANE} in our quaternary Heusler alloy CrRuXGe (X = Mn, Co) is governed by the extrinsic skew scattering mechanism. Nevertheless, the polarity of S_{ANE} for both cases (intrinsic and extrinsic origins) is primarily governed by the sign of α_{xy}^A [49].

Based on the experimental demonstration of the bipolarity of S_{ANE} in our quaternary Heusler alloys CrRuXGe (X = Mn, Co), we propose an ANE-based thermopile device configuration using these Heusler alloys at room temperature in Fig. 10(a). The ANE-based thermopile device can be fabricated by assembling several pairs of CrRuCoGe (with positive S_{ANE}) and CrRuMnGe (with negative S_{ANE}) blocks magnetized along the x direction. By applying a temperature gradient along the z direction, V_{ANE}^{Co} and V_{ANE}^{Mn} will be generated along the $+y$ and $-y$ directions in the individual CrRuCoGe and CrRuMnGe blocks, respectively. By increasing the number of CrRuCoGe and CrRuMnGe pairs (n) in the thermopile assembly, the total V_{ANE}, i.e., $V_{ANE}^{Total} = n(V_{ANE}^{Co} + V_{ANE}^{Mn})$ can be enhanced significantly [30,49,52].

Compared to conventional thermopiles based on longitudinal Seebeck thermoelectric devices which require the assembly of coupled p- and n-type legs along with complicated electrical connections on both sides of the coupled pairs [as shown in Fig. 10(b)] [30], our proposed ANE-based thermopile device using quaternary Heusler alloys consists of simple electrical connections only on one side of the thermopile assembly, which could be promising for the development of large scale ANE-based thermopile devices with highly efficient thermoelectric energy conversion.

IV. CONCLUSIONS

In summary, we have performed a comprehensive investigation of magnetic and magnetothermoelectric properties of the equiatomic quaternary Heusler alloys CrRuXGe (X = Co and Mn). Magnetic measurements reveal the presence of a glassy magnetic state owing to the energetically competing ferromagnetic and antiferromagnetic phases in CrRuCoGe at low temperatures, whereas CrRuMnGe exhibits soft FM behavior with a weak martensitic transformation close to room temperature. We find that the electron-electron elastic scattering plays a dominant role in the longitudinal electronic transport in CrRuCoGe at low temperatures in comparison to CrRuMnGe. Furthermore, while the sign of S_{xx} for the CrRuCoGe alloy is negative throughout the measured temperature range, S_{xx} for the CrRuMnGe alloy is positive, indicating electrons (holes) are the dominant carriers for the thermally driven charge transport in CrRuCoGe (CrRuMnGe). Our analysis indicates that the contribution of the magnon-drag effect in CrRuMnGe is higher than that of CrRuCoGe. Most interestingly, CrRuCoGe shows positive S_{ANE} whereas CrRuMnGe exhibits negative S_{ANE}, which has been attributed to the dominating contribution of the anomalous transverse thermoelectric conduction. Furthermore, S_{ANE} of CrRuMnGe is influenced by the martensitic transformation. Our detailed analysis indicates that the bipolar nature of ANE in both of these samples is dominated by the asymmetric skew scattering of charge carriers in the measured temperature regime. The sign change and tunability of the ANE coefficient presented in this study will pave the way for further exploration of equiatomic quaternary Heusler alloys for efficient ANE-based thermopile device applications at room temperature.

The data that support the findings of this study are available from the corresponding author upon reasonable request.

[1] G. E. W. Bauer, E. Saitoh, and B. J. Van Wees, Spin caloritronics, Nat. Mater. **11**, 391 (2012).

[2] K. Uchida, S. Takahashi, K. Harii, J. Ieda, W. Koshibae, K. Ando, S. Maekawa, and E. Saitoh, Observation of the spin Seebeck effect, Nature (London) **455**, 778 (2008).

[3] K. Uchida, J. Xiao, H. Adachi, J. Ohe, S. Takahashi, J. Ieda, T. Ota, Y. Kajiwara, H. Umezawa, and H. Kawai, Spin Seebeck insulator, Nat. Mater. **9**, 894 (2010).

[4] S. Meyer *et al.*, Observation of the spin Nernst effect, Nat. Mater. **16**, 977 (2017).

[5] S. Daimon, R. Iguchi, T. Hioki, E. Saitoh, and K. Uchida, Thermal imaging of spin peltier effect, Nat. Commun. **7**, 13754 (2016).

[6] Y. Pu, D. Chiba, F. Matsukura, H. Ohno, and J. Shi, Mott relation for anomalous Hall and Nernst effects in Ga$_{1-x}$Mn$_x$As ferromagnetic semiconductors, Phys. Rev. Lett. **101**, 117208 (2008).

[7] R. Nagasawa, K. Oyanagi, T. Hirai, R. Modak, S. Kobayashi, and K. Uchida, Anomalous Ettingshausen effect in iron–carbon alloys, Appl. Phys. Lett. **121**, 62401 (2022).

[8] K. Uchida, W. Zhou, and Y. Sakuraba, Transverse thermoelectric generation using magnetic materials, Appl. Phys. Lett. **118**, 140504 (2021).

[9] A. Ghosh, R. Das, and R. Mahendiran, Skew scattering dominated anomalous Nernst effect in La$_{1-x}$Na$_x$MnO$_3$, J. Appl. Phys. **125**, 153902 (2019).

[10] A. Ghosh, A. Chanda, and R. Mahendiran, Anomalous Nernst effect in Pr$_{0.5}$Sr$_{0.5}$CoO$_3$, AIP Adv. **11**, 35031 (2021).

[11] A. Ghosh, A. Chanda, M. Manikandan, and R. Mahendiran, Rare earth size dependence of Nernst thermopower in ferromagnetic perovskites: $R_{0.6}$Sr$_{0.4}$CoO$_3$ (R = La, Pr, and Nd), J. Magn. Magn. Mater. **537**, 168240 (2021).

[12] T. Miyasato, N. Abe, T. Fujii, A. Asamitsu, S. Onoda, Y. Onose, N. Nagaosa, and Y. Tokura, Crossover behavior of the anomalous Hall effect and anomalous Nernst effect in itinerant ferromagnets, Phys. Rev. Lett. **99**, 086602 (2007).

[13] A. Chanda, D. Rani, J. Nag, A. Alam, K. G. Suresh, M. H. Phan, and H. Srikanth, Emergence of asymmetric skew-scattering dominated anomalous Nernst effect in the spin gapless semiconductors Co$_{1+x}$Fe$_{1-x}$CrGa, Phys. Rev. B **106**, 134416 (2022).

[14] R. Ramos, M. H. Aguirre, A. Anadón, J. Blasco, I. Lucas, K. Uchida, P. A. Algarabel, L. Morellón, E. Saitoh, and M. R. Ibarra, Anomalous Nernst effect of Fe$_3$O$_4$ single crystal, Phys. Rev. B **90**, 054422 (2014).

[15] S. Isogami, K. Masuda, Y. Miura, N. Rajamanickam, and Y. Sakuraba, Anomalous Hall and Nernst effects in ferrimagnetic Mn$_4$N films: Possible interpretations and prospects for enhancement, Appl. Phys. Lett. **118**, 92407 (2021).

[16] A. De, A. K. Singh, S. Singh, and S. Nair, Temperature dependence of the anomalous Nernst effect in Ni$_2$MnGa shape memory alloy, Phys. Rev. B **103**, L020404 (2021).

[17] A. Sakai *et al.*, Giant anomalous Nernst effect and quantum-critical scaling in a ferromagnetic semimetal, Nat. Phys. **14**, 1119 (2018).

[18] S. N. Guin *et al.*, Anomalous Nernst effect beyond the magnetization scaling relation in the ferromagnetic Heusler compound Co$_2$MnGa, NPG Asia Mater. **11**, 1 (2019).

[19] D. Khadka, T. R. Thapaliya, S. Hurtado Parra, J. Wen, R. Need, J. M. Kikkawa, and S. X. Huang, Anomalous Hall and Nernst effects in epitaxial films of topological kagome magnet Fe$_3$Sn$_2$, Phys. Rev. Mater. **4**, 084203 (2020).

[20] H. Zhang, C. Q. Xu, and X. Ke, Topological Nernst effect, anomalous Nernst effect, and anomalous thermal Hall effect in the Dirac semimetal Fe$_3$Sn$_2$, Phys. Rev. B **103**, L201101 (2021).

[21] T. Asaba, V. Ivanov, S. M. Thomas, S. Y. Savrasov, J. D. Thompson, E. D. Bauer, and F. Ronning, Colossal anomalous

Nernst effect in a correlated noncentrosymmetric kagome ferromagnet, Sci. Adv. **7**, eabf1467 (2021).

[22] Z. Feng, S. Minami, S. Akamatsu, A. Sakai, T. Chen, D. Nishio-Hamane, and S. Nakatsuji, Giant and robust anomalous Nernst effect in a polycrystalline topological ferromagnet at room temperature, Adv. Funct. Mater. **32**, 2206519 (2022).

[23] H. Yang, W. You, J. Wang, J. Huang, C. Xi, X. Xu, C. Cao, M. Tian, and Z.-A. Xu, Giant anomalous Nernst effect in the magnetic Weyl semimetal $Co_3Sn_2S_2$, Phys. Rev. Mater. **4**, 024202 (2020).

[24] L. Ding, J. Koo, L. Xu, X. Li, X. Lu, L. Zhao, Q. Wang, Q. Yin, H. Lei, B. Yan, Z. Zhu, and K. Behnia, Intrinsic anomalous Nernst effect amplified by disorder in a half-metallic semimetal, Phys. Rev. X **9**, 041061 (2019).

[25] A. Chanda, J. Nag, A. Alam, K. G. Suresh, M.-H. Phan, and H. Srikanth, Intrinsic Berry curvature driven anomalous Nernst thermopower in the semimetallic Heusler alloy CoFeVSb, Phys. Rev. B **107**, L220403 (2023).

[26] C. Ran *et al.*, Anomalous Nernst effect and topological Nernst effect in the ferrimagnetic nodal-line semiconductor $Mn_3Si_2Te_6$, Phys. Rev. B **108**, 125103 (2023).

[27] J. Xu, W. A. Phelan, and C.-L. Chien, Large anomalous Nernst effect in a van der Waals ferromagnet Fe_3GeTe_2, Nano Lett. **19**, 8250 (2019).

[28] C. Fang *et al.*, Observation of large anomalous Nernst effect in 2D layered materials Fe_3GeTe_2, Appl. Phys. Lett. **115**, 212402 (2019).

[29] M. Ikhlas, T. Tomita, T. Koretsune, M.-T. Suzuki, D. Nishio-Hamane, R. Arita, Y. Otani, and S. Nakatsuji, Large anomalous Nernst effect at room temperature in a chiral antiferromagnet, Nat. Phys. **13**, 1085 (2017).

[30] Y. Pan, C. Le, B. He, S. J. Watzman, M. Yao, J. Gooth, J. P. Heremans, Y. Sun, and C. Felser, Giant anomalous Nernst signal in the antiferromagnet $YbMnBi_2$, Nat. Mater. **21**, 203 (2022).

[31] N. Nagaosa, J. Sinova, S. Onoda, A. H. MacDonald, and N. P. Ong, Anomalous Hall effect, Rev. Mod. Phys. **82**, 1539 (2010).

[32] A. Hirohata and D. C. Lloyd, Heusler alloys for metal spintronics, MRS Bull. **47**, 593 (2022).

[33] S. Tavares, K. Yang, and M. A. Meyers, Heusler alloys: Past, properties, new alloys, and prospects, Prog. Mater. Sci. **132**, 101017 (2023).

[34] S. A. Khandy and J.-D. Chai, Thermoelectric properties, phonon, and mechanical stability of new half-metallic quaternary Heusler alloys: FeRhCrZ (Z = Si and Ge), J. Appl. Phys. **127**, 165102 (2020).

[35] V. Alijani *et al.*, Electronic, structural, and magnetic properties of the half-metallic ferromagnetic quaternary Heusler compounds CoFeMn Z (Z = Al, Ga, Si, Ge), Phys. Rev. B **84**, 224416 (2011).

[36] D. Rani, Enamullah, L. Bainsla, K. G. Suresh, and A. Alam, Spin-gapless semiconducting nature of Co-rich $Co_{1+x}Fe_{1-x}CrGa$, Phys. Rev. B **99**, 104429 (2019).

[37] L. Bainsla, A. I. Mallick, M. M. Raja, A. K. Nigam, B. S. D. Ch. S. Varaprasad, Y. K. Takahashi, A. Alam, K. G. Suresh, and K. Hono, Spin gapless semiconducting behavior in equiatomic quaternary CoFeMnSi Heusler alloy, Phys. Rev. B **91**, 104408 (2015).

[38] S. Ouardi, G. H. Fecher, C. Felser, and J. Kübler, Realization of spin gapless semiconductors: The Heusler compound Mn_2CoAl, Phys. Rev. Lett. **110**, 100401 (2013).

[39] J. Nag *et al.*, CoFeVSb: A promising candidate for spin valve and thermoelectric applications, Phys. Rev. B **105**, 144409 (2022).

[40] Y. Venkateswara, S. S. Samatham, P. D. Babu, K. G. Suresh, and A. Alam, Coexistence of spin semimetal and Weyl semimetal behavior in FeRhCrGe, Phys. Rev. B **100**, 180404(R) (2019).

[41] Y. Venkateswara, J. Nag, S. S. Samatham, A. K. Patel, P. D. Babu, M. R. Varma, J. Nayak, K. G. Suresh, and A. Alam, FeRhCrSi: Spin semimetal with spin-valve behavior at room temperature, Phys. Rev. B **107**, L100401 (2023).

[42] J. Hu *et al.*, Anomalous Hall and Nernst effects in Co_2TiSn and $Co_2Ti_{0.6}v_{0.4}Sn$ Heusler thin films, Phys. Rev. Appl. **10**, 044037 (2018).

[43] C. D. W. Cox, A. J. Caruana, M. D. Cropper, and K. Morrison, Anomalous Nernst effect in Co_2MnSi thin films, J. Phys. D: Appl. Phys. **53**, 35005 (2019).

[44] A. Ghosh, A. De, and S. Nair, Large anomalous Nernst effect across the magneto-structural transition in a bulk Ni-Co-Mn-Sn full Heusler alloy, Appl. Phys. Lett. **113**, 262405 (2018).

[45] J. Hu *et al.*, Regulating the anomalous Hall and Nernst effects in Heusler-based trilayers, Appl. Phys. Lett. **117**, 62405 (2020).

[46] G. K. Shukla, U. Modanwal, and S. Singh, Nodal-line symmetry breaking induced colossal anomalous Hall and Nernst effects in Cu_2CoSn Heusler compound, Appl. Phys. Lett. **123**, 052402 (2023).

[47] Y. Sakuraba, K. Hyodo, A. Sakuma, and S. Mitani, Giant anomalous Nernst effect in the $Co_2MnAl_{1-x}Si_x$ Heusler alloy induced by Fermi level tuning and atomic ordering, Phys. Rev. B **101**, 134407 (2020).

[48] A. Chanda, D. Rani, D. DeTellem, N. Alzahrani, D. A. Arena, S. Witanachchi, R. Chatterjee, M.-H. Phan, and H. Srikanth, Large thermo-spin effects in Heusler alloy-based spin gapless semiconductor thin films, ACS Appl. Mater. Interfaces **15**, 53697 (2023).

[49] S. Noguchi, K. Fujiwara, Y. Yanagi, M.-T. Suzuki, T. Hirai, T. Seki, K. Uchida, and A. Tsukazaki, Bipolarity of large anomalous Nernst effect in Weyl magnet-based alloy films, Nat. Phys. **20**, 254 (2024).

[50] G. J. Snyder and E. S. Toberer, Complex thermoelectric materials, Nat. Mater. **7**, 105 (2008).

[51] W. Zhou, K. Masuda, and Y. Sakuraba, Origin of negative anomalous Nernst thermopower in Mn-Ga ordered alloys, Appl. Phys. Lett. **118**, 152406 (2021).

[52] Y. Sakuraba, K. Hasegawa, M. Mizuguchi, T. Kubota, S. Mizukami, T. Miyazaki, and K. Takanashi, Anomalous Nernst effect in $L1_0$-FePt/MnGa thermopiles for new thermoelectric applications, Appl. Phys. Express **6**, 33003 (2013).

[53] K. Hasegawa, M. Mizuguchi, Y. Sakuraba, T. Kamada, T. Kojima, T. Kubota, S. Mizukami, T. Miyazaki, and K. Takanashi, Material dependence of anomalous Nernst effect in perpendicularly magnetized ordered-alloy thin films, Appl. Phys. Lett. **106**, 252405 (2015).

[54] A. Sola, E. S. Olivetti, L. Martino, and V. Basso, Polycrystalline MnBi as a transverse thermoelectric material, AIP Adv. **13**, 035231 (2023).

[55] K. Ito, T. Kubota, and K. Takanashi, Negative anomalous Nernst coefficient in a Mn Al Ge film and its enhancement in a (Mn-Cr) Al Ge film, Phys. Rev. Appl. **21**, 054012 (2024).

[56] A. Miura, H. Sepehri-Amin, K. Masuda, H. Tsuchiura, Y. Miura, R. Iguchi, Y. Sakuraba, J. Shiomi, K. Hono, and K. Uchida, Observation of anomalous Ettingshausen effect and large transverse thermoelectric conductivity in permanent magnets, Appl. Phys. Lett. **115**, 222403 (2019).

[57] L. Bainsla, A. I. Mallick, M. M. Raja, A. A. Coelho, A. K. Nigam, D. D. Johnson, A. Alam, and K. G. Suresh, Origin of spin gapless semiconductor behavior in CoFeCrGa: Theory and experiment, Phys. Rev. B **92**, 045201 (2015).

[58] J. Nag, P. C. Sreeparvathy, R. Venkatesh, P. D. Babu, K. G. Suresh, and A. Alam, Nontrivial topological features and Griffith's-phase behavior in CrFeVGa probed by experiment and theory, Phys. Rev. Appl. **19**, 044071 (2023).

[59] V. Mishra, A. Kumar, L. Pandey, N. K. Gupta, S. Hait, V. Barwal, N. Sharma, N. Kumar, S. Chandra, and S. Chaudhary, Disordered spin gapless semiconducting CoFeCrGa Heusler alloy thin films on Si (100): Experiment and theory, Nanoscale **15**, 337 (2023).

[60] B. Shi, J. Li, C. Jin, J. Yang, C. Zhang, Y. Yan, Y. Wang, and G. Zhang, Distinct transport behaviors and electronic structures in Heusler alloys CoFeCrGa and CoFeCrAl, J. Magn. Magn. Mater. **517**, 167383 (2021).

[61] P. B. Prates, A. M. Maliska, A. S. Ferreira, C. M. Poffo, Z. V. Borges, J. C. De Lima, and R. S. De Biasi, Structural, thermal, and photoacoustic study of nanocrystalline Cr_3Ge produced by mechanical alloying, J. Appl. Phys. **118**, 154903 (2015).

[62] K. He, N. Chen, C. Wang, L. Wei, and J. Chen, Method for determining crystal grain size by x-ray diffraction, Cryst. Res. Technol. **53**, 1700157 (2018).

[63] S. Gupta *et al.*, Experimental observation of spin glass state in the highly disordered quaternary Heusler alloy FeRuMnGa, Phys. Rev. B **107**, 184408 (2023).

[64] K. Yadav, M. K. Sharma, S. Singh, and K. Mukherjee, Exotic magnetic behaviour and evidence of cluster glass and Griffiths like phase in Heusler alloys $Fe_{2-x}Mn_xCrAl$ ($0 \leqslant x \leqslant 1$), Sci. Rep. **9**, 15888 (2019).

[65] A. Chanda and R. Mahendiran, Sharp steps in magnetization, magnetoresistance, and magnetostriction in $Pr_{0.6}Sr_{0.4}Co_{1-y}Ga_yO_3$, Appl. Phys. Lett. **117**, 032402 (2020).

[66] J. R. L. de Almeida and D. J. Thouless, Stability of the Sherrington-Kirkpatrick solution of a spin glass model, J. Phys. A: Math. Gen. **11**, 983 (1978).

[67] J. Kroder *et al.*, Spin glass behavior in the disordered half-Heusler compound IrMnGa, Phys. Rev. B **99**, 174410 (2019).

[68] A. Kumar, S. D. Kaushik, V. Siruguri, and D. Pandey, Evidence for two spin-glass transitions with magnetoelastic and magnetoelectric couplings in the multiferroic $(Bi_{1-x}Ba_x)(Fe_{1-x}Ti_x)\,O_3$ system, Phys. Rev. B **97**, 104402 (2018).

[69] I. Galanakis, P. H. Dederichs, and N. Papanikolaou, Slater-Pauling behavior and origin of the half-metallicity of the full-Heusler alloys, Phys. Rev. B **66**, 174429 (2002).

[70] B. Govind, A. Kumar, S. Bano, R. A. Yadav, R. Gaur, K. Bir, S. Singh, and V. P. S. Awana, Investigation of magnetic behavior of non-stoichiometric $Co_{1.75}Mn_{0.5}Fe_{0.75}Si$ and $Co_{1.5}MnFe_{0.5}Si$ compositions associated with their Co_2FeSi and Co_2MnSi parent alloys, J. Magn. Magn. Mater. **574**, 170703 (2023).

[71] S. Fähler, U. K. Rößler, O. Kastner, J. Eckert, G. Eggeler, H. Emmerich, P. Entel, S. Müller, E. Quandt, and K. Albe, Caloric effects in ferroic materials: New concepts for cooling, Adv. Eng. Mater. **14**, 10 (2012).

[72] E. Hornbogen, Reversibility and hysteresis of martensitic transformations, Phys. Status Solidi **172**, 161 (1992).

[73] A. Taubel, T. Gottschall, M. Fries, S. Riegg, C. Soon, K. P. Skokov, and O. Gutfleisch, A comparative study on the magnetocaloric properties of Ni-Mn-*X*(-Co) Heusler alloys, Phys. Status Solidi **255**, 1700331 (2018).

[74] A. Aryal, I. Dubenko, S. Talapatra, A. Granovsky, E. Lähderanta, S. Stadler, and N. Ali, Magnetic field dependence of the martensitic transition and magnetocaloric effects in $Ni_{49}BiMn_{35}In_{15}$, AIP Adv. **10**, 015138 (2020).

[75] V. K. Sharma, M. K. Chattopadhyay, and S. B. Roy, Kinetic arrest of the first order austenite to martensite phase transition in $Ni_{50}Mn_{34}In_{16}$: dc magnetization studies, Phys. Rev. B **76**, 140401(R) (2007).

[76] A. Chanda, J. E. Shoup, N. Schulz, D. A. Arena, and H. Srikanth, Tunable competing magnetic anisotropies and spin reconfigurations in ferrimagnetic $Fe_{100-x}Gd_x$ alloy films, Phys. Rev. B **104**, 094404 (2021).

[77] Ö. Çakir, M. Acet, M. Farle, E. Dias, and K. Priolkar, Kinetic arrest in magnetically inhomogeneous C-deficient Mn_3GaC, J. Magn. Magn. Mater. **390**, 96 (2015).

[78] M. A. Manekar, S. Chaudhary, M. K. Chattopadhyay, K. J. Singh, S. B. Roy, and P. Chaddah, First-order transition from antiferromagnetism to ferromagnetism in $Ce(Fe_{0.96}Al_{0.04})_2$, Phys. Rev. B **64**, 104416 (2001).

[79] A. Landgraf, A. M. Jakob, Y. Ma, and S. G. Mayr, Nanoscale magneto-structural coupling in as-deposited and freestanding single-crystalline Fe_7Pd_3 ferromagnetic shape memory alloy thin films, Sci. Technol. Adv. Mater. **14**, 045003 (2013).

[80] A. G. Khachaturyan, S. M. Shapiro, and S. Semenovskaya, Adaptive phase formation in martensitic transformation, Phys. Rev. B **43**, 10832 (1991).

[81] J. P. Heremans, V. Jovovic, E. S. Toberer, A. Saramat, K. Kurosaki, A. Charoenphakdee, S. Yamanaka, and G. J. Snyder, Enhancement of thermoelectric efficiency in PbTe by distortion of the electronic density of states, Science **321**, 554 (2008).

[82] P. Mandal, Temperature and doping dependence of the thermopower in $LaMnO_3$, Phys. Rev. B **61**, 14675 (2000).

[83] J. Yang, Y. P. Sun, W. H. Song, and Y. P. Lee, Thermopower and thermal conductivity of the electron-doped manganite $La_{0.9}Te_{0.1}MnO_3$, J. Appl. Phys. **100**, 123701 (2006).

[84] A. Banerjee, S. Pal, S. Bhattacharya, B. K. Chaudhuri, and H. D. Yang, Magnetoresistance and magnetothermoelectric power of $La_{0.5}Pb_{0.5}Mn_{1-x}Cr_xO_3$, Phys. Rev. B **64**, 104428 (2001).

[85] R. Das, A. Chanda, and R. Mahendiran, Influence of magnetic field on electrical and thermal transport in the hole doped ferromagnetic manganite: $La_{0.9}Na_{0.1}MnO_3$, RSC Adv. **9**, 1726 (2019).

[86] T. M. Tritt, Thermoelectric phenomena, materials, and applications, Annu. Rev. Mater. Res. **41**, 433 (2011).

[87] J. L. Cohn, J. J. Neumeier, C. P. Popoviciu, K. J. McClellan, and T. Leventouri, Local lattice distortions and thermal transport in perovskite manganites, Phys. Rev. B **56**, R8495 (1997).

[88] J. Callaway, Model for lattice thermal conductivity at low temperatures, Phys. Rev. **113**, 1046 (1959).

[89] J. Callaway, Low-temperature lattice thermal conductivity, Phys. Rev. **122**, 787 (1961).

[90] S. Bhattacharya, A. Mehdizadeh Dehkordi, S. Tennakoon, R. Adebisi, J. R. Gladden, T. Darroudi, H. N. Alshareef, and T. M. Tritt, Role of phonon scattering by elastic strain field in thermoelectric $Sr_{1-x}Y_xTiO_{3-\delta}$, J. Appl. Phys. **115**, 223712 (2014).

[91] P. G. Klemens, Thermal resistance due to point defects at high temperatures, Phys. Rev. **119**, 507 (1960).

[92] G. A. Slack and S. Galginaitis, Thermal conductivity and phonon scattering by magnetic impurities in CdTe, Phys. Rev. **133**, A253 (1964).

[93] J. Yang, D. T. Morelli, G. P. Meisner, W. Chen, J. S. Dyck, and C. Uher, Influence of electron-phonon interaction on the lattice thermal conductivity of $Co_{1-x}Ni_xSb_3$, Phys. Rev. B **65**, 094115 (2002).

[94] F. J. DiSalvo, Thermoelectric cooling and power generation, Science **285**, 703 (1999).

[95] A. Chanda, C. Holzmann, N. Schulz, A. Ullrich, D. DeTellem, M. Albrecht, M. Gross, C. A. Ross, D. A. Arena, M.-H. Phan *et al.*, Temperature evolution of magnon propagation length in Tm3Fe5O12 thin films: Roles of magnetic anisotropy and Gilbert damping, ACS Nano **18**, 7223 (2024).

[96] A. De, A. Ghosh, R. Mandal, S. Ogale, and S. Nair, Temperature dependence of the spin Seebeck effect in a mixed valent manganite, Phys. Rev. Lett. **124**, 017203 (2020).

[97] T. Ashworth, J. E. Loomer, and M. M. Kreitman, Thermal conductivity of nylons and Apiezon greases, in *Advances in Cryogenic Engineering*, edited by K. D. Timmerhaus (Springer, Berlin, 1973), pp. 271–279.

[98] J. Holanda, O. A. Santos, R. O. Cunha, J. B. S. Mendes, R. L. Rodríguez-Suárez, A. Azevedo, and S. M. Rezende, Longitudinal spin Seebeck effect in permalloy separated from the anomalous Nernst effect: Theory and experiment, Phys. Rev. B **95**, 214421 (2017).

[99] D. Kan and Y. Shimakawa, Strain effect on thermoelectric properties of $SrRuO_3$ epitaxial thin films, Appl. Phys. Lett. **115**, 022403 (2019).

[100] W.-L. Lee, S. Watauchi, V. L. Miller, R. J. Cava, and N. P. Ong, Anomalous Hall heat current and Nernst effect in the $CuCr_2Se_{4-x}Br_x$ ferromagnet, Phys. Rev. Lett. **93**, 226601 (2004).

[101] N. F. Mott, and H. Jones, *The Theory of the Properties of Metals and Alloys* (Dover Publications, Mineola, NY, 1958).

[102] X. Li, L. Xu, L. Ding, J. Wang, M. Shen, X. Lu, Z. Zhu, and K. Behnia, Anomalous Nernst and Righi-Leduc effects in Mn_3Sn: Berry curvature and entropy flow, Phys. Rev. Lett. **119**, 056601 (2017).

[103] A. K. Singh and G. K. Shukla, and S. Singh, Intrinsic anomalous Hall conductivity and real space Berry curvature induced topological Hall effect in Ni_2MnGa magnetic shape memory alloy, J. Phys. D: Appl. Phys. **56**, 044004 (2022).

[104] Y. Hamada, Y. Kurokawa, T. Yamauchi, H. Hanamoto, and H. Yuasa, Anomalous Nernst effect in Fe–Si alloy films, Appl. Phys. Lett. **119**, 152404 (2021).